On the Dynamics of the Southern Senegal Upwelling Center: Observed Variability from Synoptic to Superinertial Scales

Xavier Capet,[a] Philippe Estrade,[b] Eric Machu,[b,c] Siny Ndoye,[b,a] Jacques Grelet,[d]
Alban Lazar,[a] Louis Marié,[c] Denis Dausse,[a] and Patrice Brehmer[e,f]

[a] LOCEAN Laboratory, CNRS-IRD-Sorbonne Universités, UPMC, MNHN, Paris, France
[b] Laboratoire de Physique de l'Atmosphère et de l'Ocean Siméon Fongang, ESP/UCAD, Dakar, Senegal
[c] Laboratoire d'Océanographie Physique et Spatiale, IRD-CNRS-IFREMER-UBO, Plouzané, France
[d] Institut de Recherche pour le Développement, US 191 IMAGO, Plouzané, France
[e] Institut Sénégalais de Recherche Agronomique, Centre de Recherche Océographique Dakar-Thiaroye, Dakar, Senegal
[f] Laboratoire des Sciences de l'Environnement Marin (UMR 195 LEMAR; IRD-CNRS-UBO-Ifremer), Dakar, Senegal

ABSTRACT

Upwelling off southern Senegal and Gambia takes place over a wide shelf with a large area where depths are shallower than 20 m. This results in typical upwelling patterns that are distinct (e.g., more persistent in time and aligned alongshore) from those of other better known systems, including Oregon and Peru where inner shelves are comparatively narrow. Synoptic to superinertial variability of this upwelling center is captured through a 4-week intensive field campaign, representing the most comprehensive measurements of this region to date. The influence of mesoscale activity extends across the shelf break and far over the shelf where it impacts the midshelf upwelling (e.g., strength of the upwelling front and circulation), possibly in concert with wind fluctuations. Internal tides and solitary waves of large amplitude are ubiquitous over the shelf. The observations suggest that these and possibly other sources of mixing play a major role in the overall system dynamics through their impact upon the general shelf thermohaline structure, in particular in the vicinity of the upwelling zone. Systematic alongshore variability in thermohaline properties highlights important limitations of the 2D idealization framework that is frequently used in coastal upwelling studies.

1. Introduction

Coastal upwelling systems have received widespread attention for several decades owing to their importance for human society. Although the primary driving mechanism is generic, important differences exist between systems and also between sectors of each given system. Stratification, shelf/slope topographic shapes, coastline irregularities, and subtleties in the wind spatial/temporal structure have a major impact on upwelling water pathways and overall dynamical, hydrological, biogeochemical (Messié and Chavez 2015), and ecological (Pitcher et al. 2010) characteristics of upwelling regions. Over the past decade processes associated with short time scales (daily and higher) have progressively been incorporated into our knowledge base, adding further complexity as we account for local specifics.

These advances have to a large extent taken place in the California Current System (Woodson et al. 2007, 2009; Ryan et al. 2010; Kudela et al. 2008; Lucas et al. 2011a) and to a lesser extent in the Benguela system (Lucas et al. 2014). Conversely, our understanding of West African upwellings remains to a large extent superficial (i.e., guided by satellite and sometimes surface in situ measurements; Roy 1998; Demarcq and Faure 2000; Lathuilière et al. 2008), low frequency, and relatively large scale. A notable exception is Schafstall et al. (2010) with an estimation of diapycnal nutrient fluxes due to internal wave dissipation over the Mauritanian shelf.

The large-scale dynamics and hydrology of the southern end of the Canary system has, on the other hand, been known for a long time (Barton 1998). Between the Cape Verde frontal zone [which runs approximately
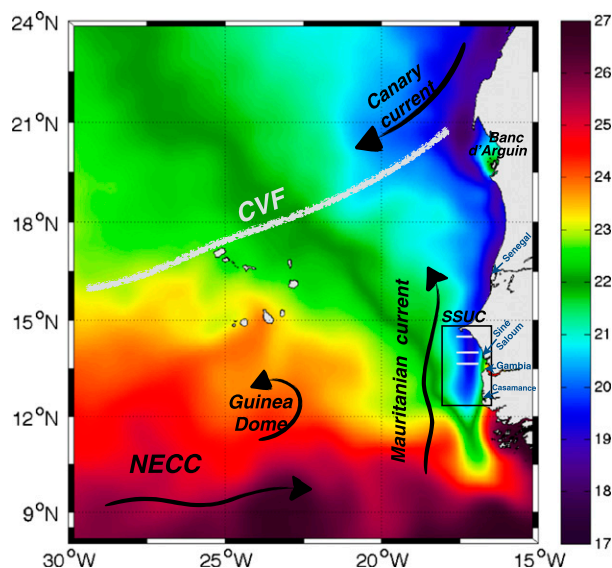
FIG. 1. Averaged Operational SST and Sea Ice Analysis (OSTIA) composite SST over the northeastern tropical Atlantic for the period 21 Feb–18 Mar 2013 corresponding to the UPSEN2–ECOAO field experiments. The image was produced by averaging daily fields downloaded online (from ftp://data.nodc.noaa.gov/pub/data.nodc/ghrsst/L4/GLOB/UKMO/OSTIA). Superimposed is a schematic representation of the main circulation features of the region including the North Equatorial Countercurrent (NECC) and the Cape Verde frontal zone (CVF, thick gray). Our study area, the SSUC (black box), stands out as the southern tip of the coastal upwelling system. White zonal lines indicate the location of our three main hydrological transects.

between Cape Blanc (~21°N, Mauritania) and the Cape Verde Archipelago (see Fig. 1)] and Cape Roxo (12°20′N), the wind regime is responsible for quasi-permanent Ekman pumping and winter/spring coastal upwelling. The former extends hundreds of kilometers offshore and drives a large-scale cyclonic circulation whose manifestation includes the Mauritanian Current (MC hereinafter; see Fig. 1). The MC differs from poleward undercurrents typical of many upwelling systems in that it is generally intensified at or close to the surface (Peña-Izquierdo et al. 2012; Barton 1989), reflecting the strength of the forcing. In the south, the MC connects with the complex equatorial current system, and the connection involves a quasi-stationary cyclonic feature: the Guinea Dome [more details can be found in Barton (1998) and Aristegui et al. (2009)]. Figure 1 is suggestive of the role of the MC in maintaining a relatively warm environment in the immediate vicinity of the shelf break over the latitude band 12°–17°N, despite sustained coastal upwelling.

Seasonality of hydrology and circulation of the coastal ocean off this part of West Africa are tightly controlled by the displacements of the intertropical convergence zone (Citeau et al. 1989). During the monsoon season

(July–October) weak westerly winds (interrupted by the passage of occasional storms and easterly waves) dominate and the region receives the overwhelming fraction of its annual precipitation. From approximately November to May the ITCZ is located to the south and upwelling-favorable trade winds dominate. Their peak intensity is in February–April, our period of interest, during which precipitation and river runoff is insignificant.

Two coastal sectors can be distinguished in this region, based on distinctions between their atmospheric forcings, influence of the surrounding ocean, and shelf/slope morphology. North of the Cape Verde Peninsula the shelf is relatively narrow (up to the Banc d'Arguin at ~20°N) and, because this is the northern limit of the ITCZ migration, the upwelling season here is longest.

This study reports and analyzes observations carried out in the southern sector offshore of southern Senegal (between the Cape Verde Peninsula and ~13°40′N; see Fig. 1) during two consecutive field experiments (amounting to 25 days at sea) carried out in February–March 2013, that is, the core of the upwelling season. The general strategy was to cover a relatively limited area of ~1° by 1° (Fig. 1) multiple times, taking measurements of physical, biogeochemical, and ecological parameters. We herein focus on the physics, but the role of this coastal region as fishing ground and small pelagic fish nursery is an important motivation for this work.

During the upwelling season, the southern sector acts as an upwelling center referred to as southern Senegal upwelling center (SSUC) below. The terminology ''upwelling center'' refers to the existence of a well-identified and persistent focal point where upwelling is enhanced and from which a cold tongue originates, as vividly revealed by SST images (Fig. 1). In upwelling systems with intense mesoscale turbulence, cold upwelling tongues take the form of filaments that are predominantly directed toward the slope and open ocean (Strub et al. 1991) and thus strongly contribute to cross-shore exchanges. Mesoscale activity is not particularly intense in the Canary system (Capet et al. 2008b; Marchesiello and Estrade 2009). In addition, the SSUC is mostly characterized by a wide shelf. South of 14°30′N, the shelf break, roughly defined by the 100-m isobath, is 50 km away from shore or more, while water depth is less than 30 m over ⅓ to ½ of the shelf area (e.g., see Fig. 3). Thus, coastal upwelling in the SSUC is partly sheltered from the mesoscale influence taking place over the continental slope and open ocean. This has several related implications: the general orientation of the cold upwelling tongue is north to south and, judging from SST images, it preserves its coherence over long distances (up to 300–400 km in some circumstances;

Ndoye et al. 2014);[1] temporal stability of the tongue is also noticeable over periods of many days to weeks; and export from the shelf to the open ocean is retarded.

This being said, the degree of insulation between shelf upwelling dynamics and offshore turbulent activity needs to be qualified. South of 14°30′N, the upwelling tongue is frequently found 50 km or more away from the coast. Its offshore edge, generally referred to as the upwelling front, is then within the range of influence of large slope/shelfbreak eddies and meanders whose surface expressions are frequently seen impinging on the outer shelf (Ndoye et al. 2014). Such situations occur preferentially between February and April and prevailed during our observational period.[2]

The process underlying the offshore migration of the upwelling tongue is present and well understood in 2D across-shore/vertical (2DV) models. The key dynamical feature of 2DV models subjected to upwelling-favorable winds is the upwelling front. Under such idealizations, the upwelling front possesses several defining characteristics (Allen et al. 1995; Austin and Lentz 2002; Estrade et al. 2008): it is the physical barrier between offshore non-upwelling and cold upwelling waters, that is, it is the place of maximum surface density gradient (this can also be true for other tracers); it is the place of maximum equatorward alongshore velocity; it coincides with the main pycnocline outcrop (Austin and Barth 2002); and low/vanishing stratification should be found on its inshore flank, that is, the upwelling zone where cold interior waters are incorporated into the surface layer.

Coalescence between the surface and bottom boundary layers has traditionally been invoked as the main explanation for the displacement of the upwelling front away from the shoreline (Estrade et al. 2008; Austin and Lentz 2002). In the alongshore momentum balance the maintenance of well-mixed, inner-shelf waters implies a compensation between wind and bottom friction with little or no offshore Ekman transport needed. Therefore, coastal divergence is expected to take place where water is deep enough for the two boundary layers to separate, typically 15 to 40 m depending in part on wind intensity (stronger winds lead to both thicker surface boundary layers and thicker bottom boundary layers because they tend to increase the strength of the upwelling jet (UJ) as confirmed by the observations described below). In the SSUC the migration of the upwelling tongue on seasonal scales (very close to shore in the early season, farthest offshore in March when upwelling winds are strongest, and retreating back inshore in April–May) is consistent with the cycle of upwelling wind intensity (Ndoye et al. 2014). On the other hand, analysis of SSUC SST also shows cold upwelling tongue behavior (in terms of zonal position and displacements) that is suggestive of other processes being at play. Farther north, over a wide continental shelf resembling the SSUC, Barton et al. (1977) observe an upwelling front that migrates offshore during two consecutive upwelling events without any evident relation to changes in wind intensity. Similar behavior will be described below for the SSUC. Overall, the connection between cross-shore migration of the upwelling zone and wind intensity is unclear, at least on synoptic time scales.

The purpose of this study is to better understand the dynamics underlying upwelling front evolutions and, more generally, shed light on the dynamics of the SSUC. As we will see, other aspects of the 2DV conceptual model that have traditionally been used to investigate the SSUC dynamics need serious reconsideration in the light of the Upwelling du Sénégal 2 (UPSEN2)–Écosystèmes de l'Afrique de l'Ouest (ECOAO) observations. Identification of the upwelling front during these experiments is frequently ambiguous, and, when possible, the upwelling front rarely satisfies all of the characteristics laid out above. Also, limited sampling of the inshore edge of the upwelling tongue suggests that warmer coastal waters were overwhelmingly stratified during the experiments; hence, the 2DV view of the offshore migration of the upwelling tongue does not seem to be relevant.

On the other hand, our observations provide multiple pieces of evidence pointing to the importance of complex-scale interactions in the SSUC. Shelfbreak/open-ocean mesoscale disturbances and superinertial dynamics (e.g., internal gravity waves) exert a fundamental influence on the SSUC dynamics, thermohaline structure, and, in particular, on the position and shape of the upwelling tongue.

The manuscript is organized as follows: Section 2 presents the data and methods. Section 3 describes the synoptic evolution of the SSUC state and circulation

---

[1] Note, however, that incorporation of subsurface water in the tongue tens to hundreds of kilometers from its northern origin near Dakar cannot be ruled out. In other words the concept of a wake, within which upwelled water in a confined northern area would simply be advected southward, may not be applicable. In that respect, the cold tongue may be distinct from upwelling filaments present in other upwelling sectors in which the key dynamical process is subduction of recently upwelled water as it flows offshore past the shelf break.

[2] The seaward displacement of the cold tongue is accompanied by the establishment of a nearshore, warm-water strip south of ~14°20′N that has historically attracted much attention because it is, intuitively, favorable to the retention of eggs and larvae of marine species (Demarcq and Faure 2000). The shallow and poorly charted area where this warm strip is found was considered unsafe for the R/V Antéa. Therefore, just a small number of observations were made at the edge of this strip, which does not allow us to properly analyze its dynamics.

during the field experiments. Emphasis is placed on the midshelf area where moored instruments allow us to better characterize the dynamics. The flow regime and submesoscale activity are also briefly examined. In section 4, a set of observations is presented from ship echosounders and moored instruments that suggests the dynamical importance of the SSUC internal wave field. The final section summarizes and elaborates on our findings and their consequences.

2. Data and methods

a. Moored instruments

A string of instruments (hereinafter referred to as M28) was deployed in about 28-m water depth at 14°N, 17°06′W on 23 February (0800 UTC) and recovered on 12 March (1500 UTC). It consisted of 8 temperature T sensors and 10 temperature, salinity S, and pressure sensors with a 1-min sampling interval. Measurements made by the 18 T sensors are used to obtain a temperature time–depth gridded field (described in sections 3 and 4). This is achieved through objective analysis (Bretherton et al. 1976), using 1 m and 2 min for the vertical and time resolution of the grid and 1 m and 4 min for the decorrelation depth and time scale. The decorrelation time scale is chosen so that internal wave signals with periods of ~10 min or more are preserved.

Three upward-looking ADCP moorings were also deployed 0.5 nm west and east (RDI 300 kHz respectively referred to as RDIW and RDIE) and south [Aquadopp 400 kHz (AQDS)] of the thermistor line. Mean water depth at the moorings ranged from approximately 29 (RDIW) to 26.5 m (RDIE). One additional ADCP Aquadopp 600 kHz (AQDI) was moored a few miles to the east in 23-m depth. Deployment of the ADCPs took place on 22 February between 1020 and 1210 UTC. Recovery took place on 12 (RDIW) or 15 March. RDI (Aquadopp) ADCPs sampled every 2 min (5 min) with vertical resolution of 1 m. Accounting for the depth at which the instrument's head was located ($\approx$0.5 m above ground) and a 1-m blanking distance, the lowest valid measurement is centered at 2 m above the bottom. Because of sidelobe reflection from the air–sea interface, the shallowest useable bin is centered at 5-m depth. The barotropic component of measured currents was detided using the software T_Tide (Pawlowicz et al. 2002). M_2 is by far the dominant constituent (not shown).

b. Hydrographic measurements

Zonal (approximately across shore) CTD transects were repeated at 14°, 14°30′, and 13°40′N during the surveys and additional yoyo CTD stations were also

performed. Data were acquired using a SBE911+, redundantly measuring pressure, temperature, and conductivity at 24 Hz and fluorescence and oxygen at 2 Hz. Data postprocessing was performed using the SeaBird SBE processing software and follows standard practices as described in many studies (see, e.g., Morison et al. 1994). Only the downcast profiles are used for analysis; during the upcast sensors are in the wake of the package and CTD frame (Alford and Pinkel 2000). Raw pressure is filtered using a 15-point triangle window. This is enough to eliminate all pressure reversals despite the relatively low drop speed we chose to increase vertical resolution (0.5 m s^{-1}). We attribute this to CTD operation through a moon pool located toward the center of R/V *Antéa*, which limits heave effects. Sea states were also favorable with limited swell in the area. A 5-point median filter is applied to temperature and salinity. A correction for the conductivity cell thermal mass (Morison et al. 1994) is also applied, requiring the knowledge of two parameters α (initial amplitude) and τ (time scale) that characterize conductivity measurement error when instantaneously applying a 1°C step in temperature. SBE default values were checked and slightly modified using a series of profiles exhibiting abrupt T jumps at the interface of a well-mixed, 20–30-m-thick bottom layer (not shown). The salinity profile closest to a step was obtained for $\alpha = 0.025$ and $\tau = 7$ s, and these values are used for all CTD profiles. For most purposes including the construction of hydrological transects, depth averaging is performed over 1-m bins. Bin size is reduced to 0.15 m to construct yoyo CTD profiles used to estimate dissipation and mixing intensity, through the computation of Thorpe scales (section 4). This roughly corresponds to seven scans at the drop speed of 0.5 m s^{-1}.

Alongtrack surface temperature and salinity are available from the SBE21 ship thermosalinometer (TSG data hereinafter).

c. Ancillary measurements

R/V *Antéa* is equipped with a four-frequency scientific echosounder SIMRAD EK60 (38, 70, 120, and 200 kHz). The ping rate is 1 Hz, which yields a 3.5-m native resolution for the echograms when the ship steams at 8 knots (kt; 1 kt = 0.51 m s^{-1}).

The weather station onboard R/V *Antéa* (Batos 1.1D) provides wind speed and direction measured at approximately 20-m height. To minimize the effect of airflow distortion by the ship superstructure, measurements corresponding to aft wind conditions are systematically discarded. Hourly wind at the Yoff weather station at Dakar Airport, Senegal (14°44′N, 17°30′W, 27 m above ground; hereinafter DWS) are obtained

online (from http://www.ogimet.com/metars.phtml.en). ASCAT scatterometers onboard *Meteorological Operational* (*MetOp*)-*A* and *MetOp-B* provide 2D wind measurements between zero and three times a day, around 1030 and/or 2230 UTC. We use the 12.5-km L2 products from NASA and present these observations after spatial averaging over different subdomains of the SSUC.

We use L2 Moderate Resolution Imaging Spectroradiometer (MODIS) onboard the *Terra* and *Aqua* satellites distributed by NASA (http://oceancolor.gsfc.nasa.gov). The metric ground resolution varies depending on view angle but remains close to the nominal 1-km value. Cloud masking produces numerous false positives in upwelling regions, and we instead rely on visual examination over the SSUC to keep or discard images.

3. Subinertial SSUC dynamics

Several types of observations, presented below, give complementary perspectives on the physical situation during the campaigns and, particularly, on the sequence of synoptic events.

a. Synoptic variability

DWS is generally quite representative of synoptic wind conditions over the SSUC, especially in situations where northwesterlies dominate (Ndoye et al. 2014), as during UPSEN2–ECOAO. Analysis of DWS wind records (Fig. 2a) suggest three coherent subperiods: a moderate relaxation period RL1 from the beginning of the cruise (22 February) to 27 February when the wind over the previous inertial period is back to above 5 m s^{-1}; 28 February to 12 March (UP1) during which the wind intensity remains essentially between 5 and 7 m s^{-1}; and from 12 March to 17–18 March during which another relaxation period RL2 takes place that, beside a more rapid initiation and a longer duration (~5 days vs 3–4 days), resembles the earlier one RL1. The short upwelling event that took place around 20–21 February just before UPSEN2 is referred to as UP0.

This description of DWS winds is broadly consistent with ship weather station observations made within 50 km of M28 reported in Fig. 2d. For example, the weakest (strongest) ship winds are found on 25 February and 15 March (28 February and 8 March). This being said, limited coverage at M28 and significant intradaily variability tend to overshadow the synoptic signal and curtail a detailed comparison. In particular, daily wind cycles differ at M28 and DWS. During most of the experiment, upwelling wind intensity at M28 peaks in the evening or early at night and is at minimum around midday (Fig. 2e). Also note that upwelling events seem to manifest themselves through increased maximum wind intensities at M28, while morning winds remain generally weak. The daily wind cycle has a much lower amplitude at DWS and maximum wind intensity occurs around 1400 UTC (see Ndoye et al. 2014).

In Fig. 2b, we show the zonal minimum temperature over the shelf averaged over the latitudinal range 14°–14°30′N, computed for all cloud-free MODIS SST images (a subset of these images is presented in Fig. 3). The upwelling event finished around the beginning of UPSEN2 UP0; the short relaxation period RL1, central upwelling event UP1, and final relaxation RL2 are clearly identifiable as SST fluctuations of ~2°–3°C. The termination date of RL1 cannot be determined precisely in SST because no MODIS SST is available on 25 and 26 February, but declining temperatures on 27–28 February approximately coincide with the increase in upwelling wind intensity. As for the SST warming during the late part of the observation period, its initiation around 8 March precedes the marked wind drop on 12–13 March by around 4 days. We will come back to this discrepancy when presenting midshelf variability. In SST RL2 is most marked on 17 March, that is, upon the return of more favorable upwelling wind conditions.

Overall, the storylines based on DWS winds or synoptic evolution of the system SST are in good agreement, considering the sampling limitations and complexity of the ocean response to wind changes.

b. SSUC mesoscale variability

With over 50 nearly cloud-free images over the duration of the experiment, MODIS provides invaluable information on the state and synoptic variability of the SSUC at scales of a few kilometers and larger.

Most images exhibit the patterns typical of the SSUC during the upwelling season, namely, the presence of a tongue of cold water whose source is situated just south of Dakar (where the coldest waters are found) and extends southward over the shelf, with some warmer waters being found offshore but also inshore of the tongue south of 14°30′N. Southward attenuation of the cold signal strongly varies with time.

During the entire experiment, the frontal zone between the cold upwelling water and warmer offshore water is distorted and forms filaments and meanders of typical size ~20–100 km, some of which acquire quasi-circular shapes (Fig. 3). As demonstrated for other upwelling systems these mesoscale structures must be the manifestation of baroclinic–barotropic instability (Marchesiello et al. 2003). The tendency of filaments to orient themselves along a northwest–southeast axis (Figs. 3e–h) reflects the intense lateral shear (partly
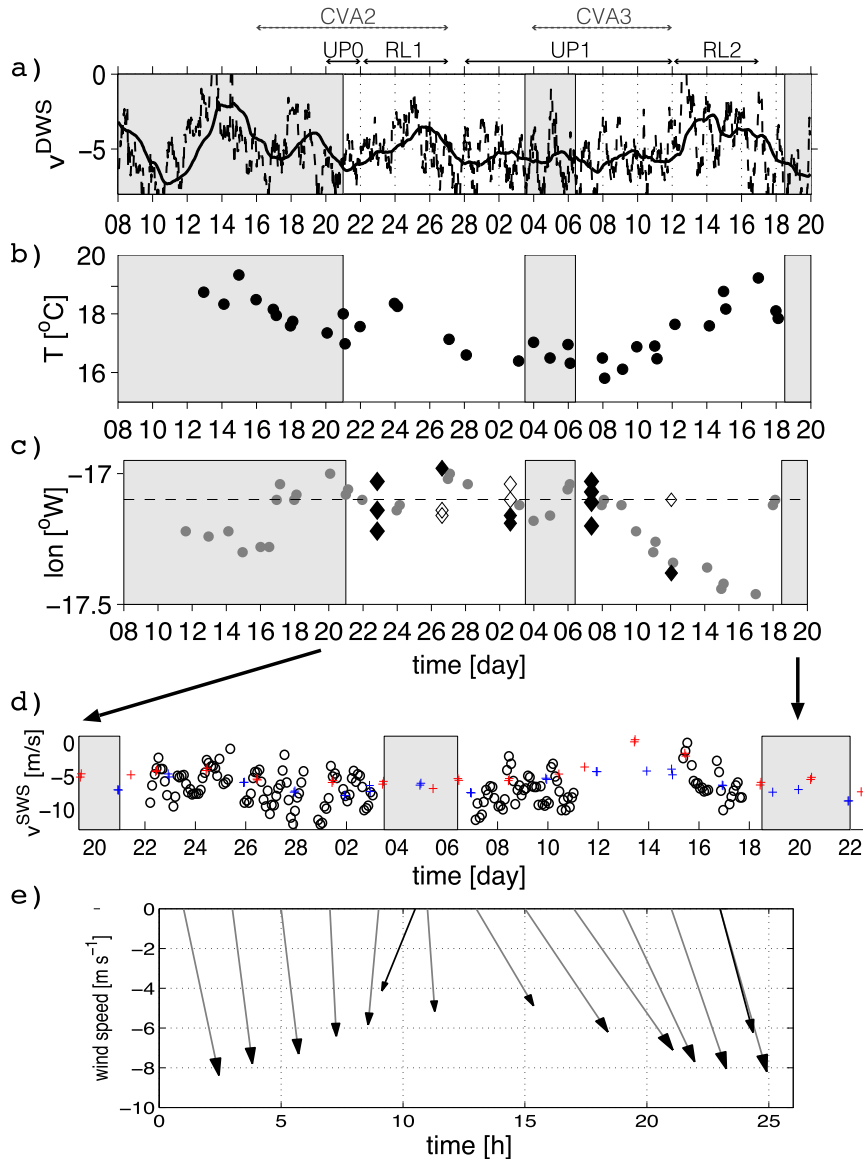
FIG. 2. (a) Instantaneous (dashed) and low-pass filtered with one inertial period forward shift (solid black) meridional wind at DWS (m s^{-1}; negative is southward). (b) MODIS zonal minimum of nighttime SST averaged meridionally over the northern SSUC (14°–14°30′N). This time series index is insensitive to cross-shore displacements of the upwelling zone. (c) Longitude of the SST zonal minimum in the latitude range 14°N ± 10′. Gray dots are estimated from MODIS cloud-free L2 images. Black diamonds are SST minima present in TSG temperature along the 14°N transect. Secondary minima that are less than 0.1°C (0.3°C) warmer than the coldest SST are also indicated with identical (open) diamonds. M28 longitude is indicated with the dashed line. (d) 2-hourly averaged meridional wind measured by the ship weather station when the ship mean position is within 50 km from M28. ASCAT measurements within 50 km from M28 (area averaging) are also shown as red (blue) crosses for daytime (nighttime) data. (e) Diurnal wind cycle computed from all ship measurements made within 50 km from M28 (arrows with gray lines). Morning and evening ASCAT winds for the same period and domain are also represented (black arrows at 1040 and 2240 UTC). In (a)–(d), abscissa are days from the beginning of the month (February or March). Gray rectangles delineate the periods with no shipboard measurements.
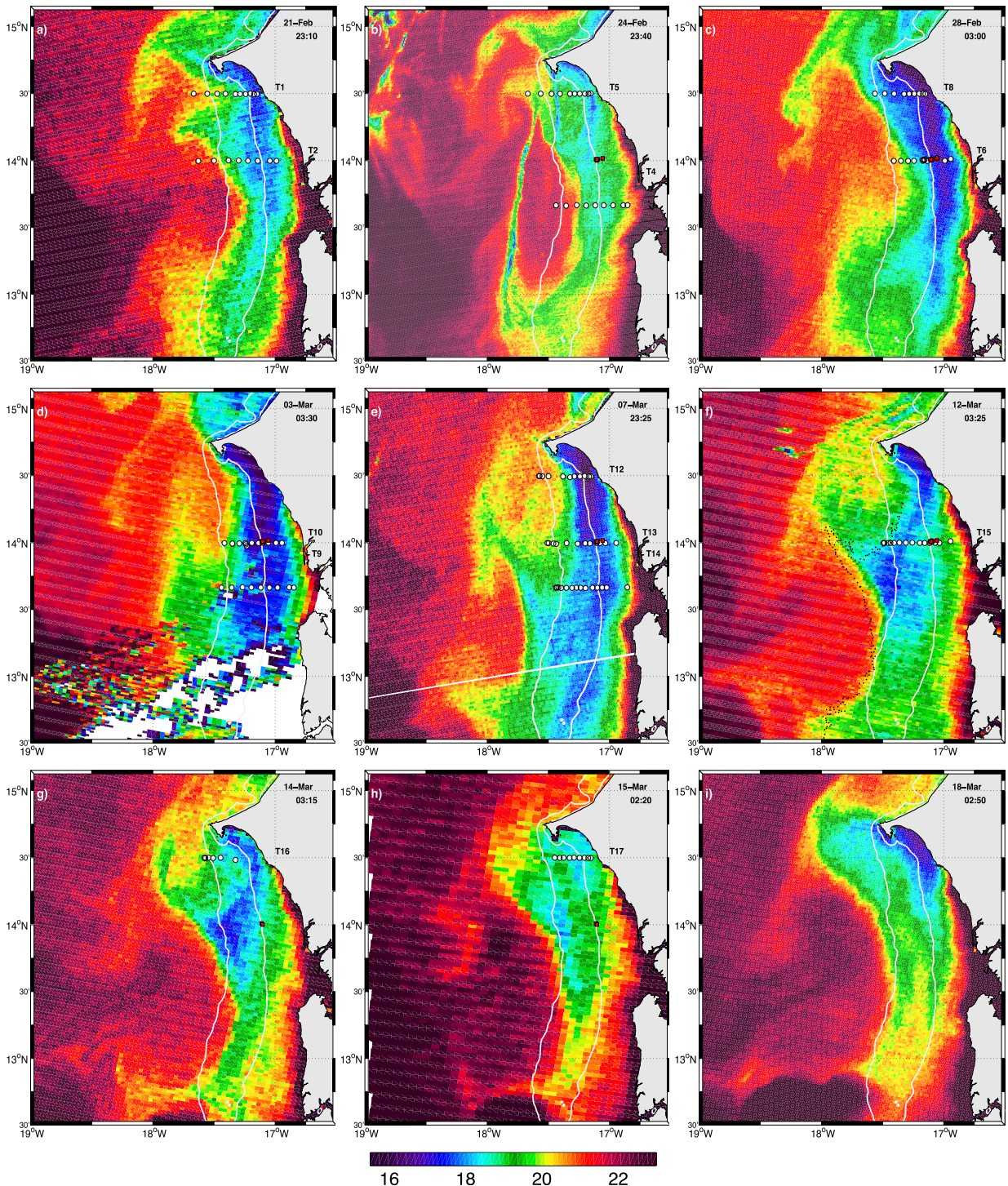
FIG. 3. MODIS SST at different times (given in upper-right corner of each image) during the experiments. CTD transects carried out within 1.5 day (prior or after) of the scene are indicated with white dots and labeled on land. Mooring locations are indicated with red square markers when they are deployed at the time of the scene. The 30- and 100-m isobath are drawn as white lines. Small areas possibly contaminated by clouds are not flagged, for example, along the line that joins [13°30′N, −18°W and Cape Verde in (b)]. Black dots in (f) represent the position of the 20°C contour on 2300 UTC 9 Mar, that is, about 2 days before the scene.

resolved by our across-shore sections; see below) between the poleward Mauritanian Current and the inshore equatorward upwelling flow.

In their analysis of the MODIS SST database, Ndoye et al. (2014) identify a recurrent mesoscale situation when a 30–100-km anticyclone [referred to as the Cape Verde anticyclone (CVA) structure] hugs the Cape Verde headland. In February–March 2013 three different CVAs consecutively occupy the northern SSUC following a sequence of events involving 1) northward propagation and deformation/amplification of a Mauritanian Current meander initially situated farther south; 2) phase locking or reduced propagation of the meander, which remains in the immediate vicinity of the Cape Verde headland for several days while taking a more circular shape; and 3) weakening/shrinking of the structure in a fashion that suggests mixing between warm waters in the CVA core and colder waters.

At the beginning of UPSEN2 (21–23 February) the remains of a small CVA (CVA-2) more easily identified at earlier times (18 February, not shown) are still visible 50 km to the south-southwest of Cape Verde (Fig. 3a). On 27 February (Fig. 4), the SST signal of CVA-2 has mostly faded. The SST scene for 28 February (Fig. 3c) captures the transient situation when ~18°C water occupies the vicinity of Cape Verde and warmer water is located ~30 km farther offshore. It also reveals the final stage of the evacuation of CVA-2, which has been stirred beyond recognition in the deformation region near 14°45′N, 17°45′W, and the northward progression of the frontal edge oriented northwest–southeast that separates a warm MC meander from upwelling water between 13°40′N and 14°50′N (cf. Figs. 3b and 3c). This frontal zone had remained quasi stationary from 21 to 24–25 February. By 3 March, it has shifted considerably farther north (Fig. 3d). It is then located partly north of and in close contact with Cape Verde. The northern and southern parts of the front evolve somewhat independently thereafter. North of Cape Verde, the front progresses northward and forms a barrier to cold upwelled water (Fig. 3e), even right at the coast where SSTs are systematically warmer than 20°C during UP1. South of Cape Verde the front combines with a ~20°C water filament located at 17°45′–18°W to form the quasi-circular edge of a mesoscale structure (CVA-3) between 5 and 10–12 March (Figs. 3e,f).

The SST signature of CVA-3 is progressively eroded, particularly at its eastern side as seen on 12 March (Fig. 3f). On 14 March (Fig. 3g), the remains of CVA-3 are barely visible as a bulge of ~20°C water near 14°30′N, 17°45′W. Later on, during RL2 (Figs. 3h,i), SST images reveal a major reorganization of the flow structure in the vicinity of the Cape Verde Peninsula. The

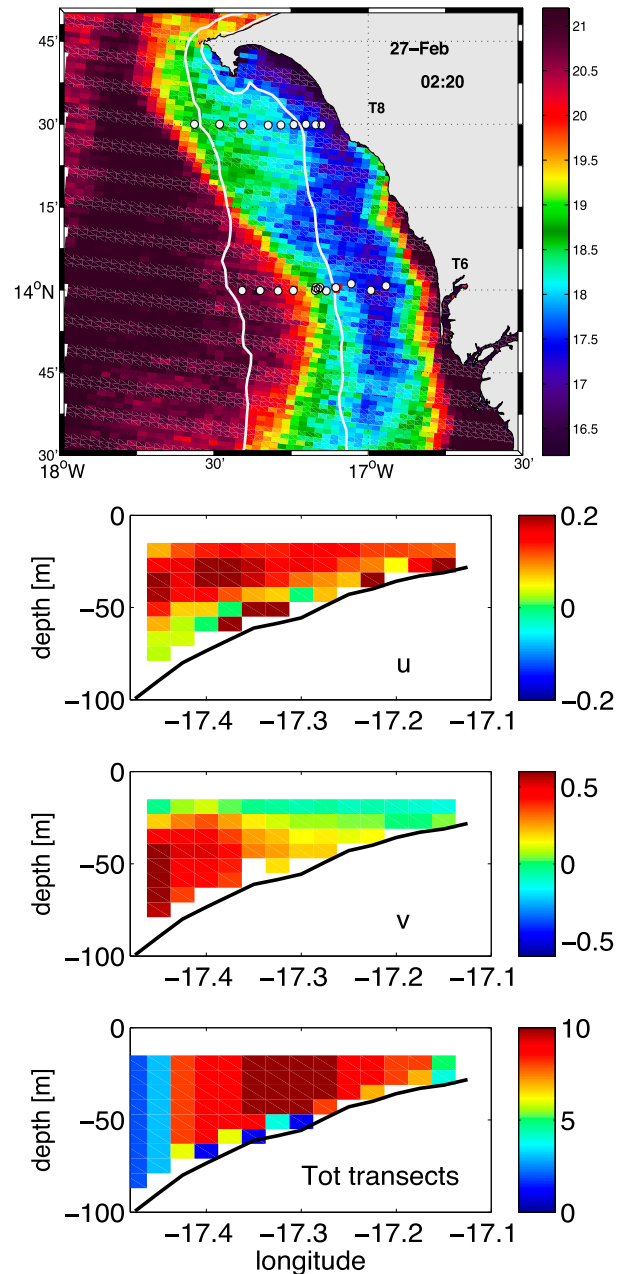FIG. 4. (top) MODIS SST and (middle) ship ADCP velocities (across shore u, alongshore v) around 27 Feb during an episode of intense onshore flow. (bottom)The number of individual transects contributing to every binned velocity data is also indicated.

upwelling signature on SST is confined to the northern SSUC (note that the maintenance of some upwelling is consistent with DWS and ship wind records; see Fig. 2). The orientation of the wake of waters upwelled at the Cape Verde Peninsula suggests that the surface flow is directed offshore on 18 March in the region between the coast and a subsequent warm meander still situated
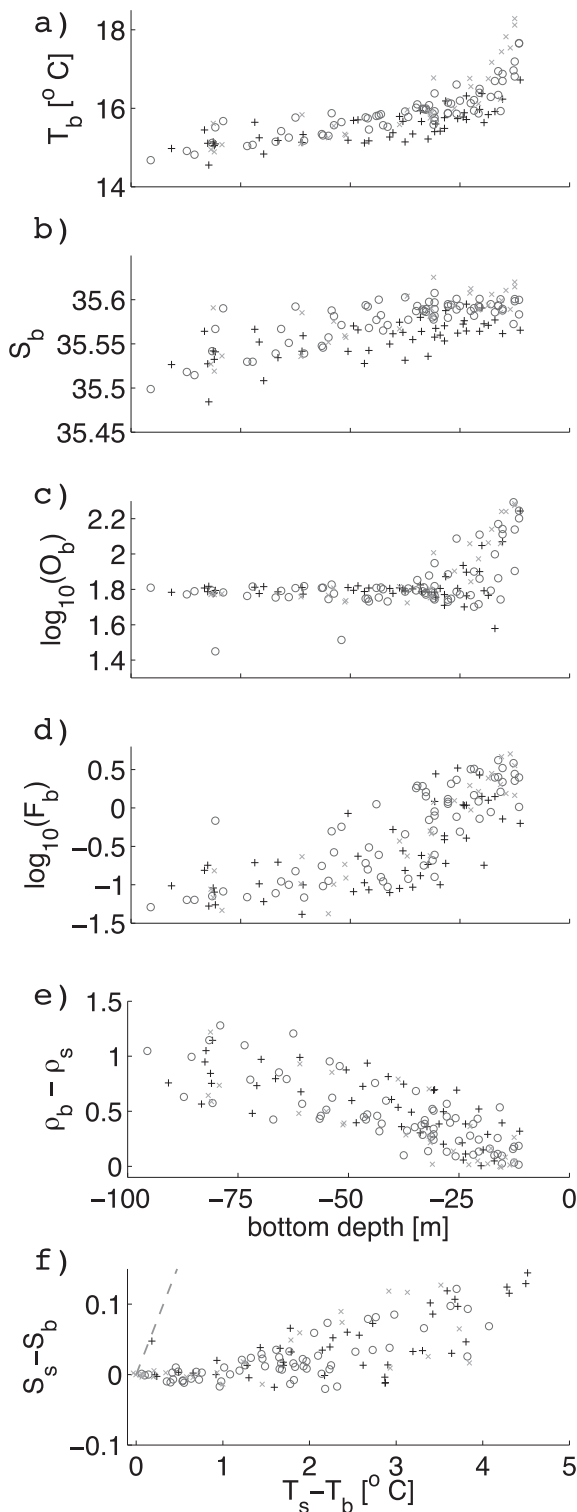
approximately 50 km offshore to the southwest (Fig. 3i). VIIRS ocean color images available for 17 and 18 March further support the onset of an offshore surface flow in the northern SSUC toward the end of RL2 (not shown).

The mesoscale features described above are typically located over the continental slope, but they also frequently extend onto the shelf as described below using in situ observations. Their evolution is tied to that of the SSUC cold tongue over the shelf, for example, through upwelling filaments. Pending modeling sensitivity analyses, our conceptual view of the SSUC dynamics is that offshore and shelf dynamics are coupled through the instabilities of the shelf/shelfbreak/slope current system. Synoptic variabilities of the MC transport and of the wind-induced shelf circulation are a priori important sources of modulation for these instabilities.

c. Subsurface properties and thermohaline structure

The set of CTD casts carried out during the experiments offer important subsurface information. In particular, they allow us to examine the properties of the cold subsurface water that feeds the upwelling and its relation to SST. Stratification is also useful as a signature of mixing. Figure 5 represents the across-shelf distribution of temperature, salinity, dissolved oxygen, and fluorescence in the bottom layer and surface to bottom density difference. Figures 6 and 7 represent T and S along 13 of the 17 main cross-shore transect lines.

All transects exhibit the signature of cold (14°–15°C) and fresh bottom water, with low dissolved oxygen and fluorescence properties, rising up the shelf to feed the Ekman divergence. T–S properties and, in particular, low subsurface salinity are typical of the South Atlantic Central Water (Hughes and Barton 1974; Peña-Izquierdo et al. 2012). A remarkable trait of this signature is that it tends to fade away when approaching the shore, although to various degrees depending on the transect and the tracer. The southern transects (T4, T9, and to a lesser extent T14) exhibit the most pronounced changes in bottom water T and S properties across the shelf. The northern transects (at 14°30′N) T1 and T12

FIG. 5. Bottom (a) temperature, (b) salinity, (c) dissolved oxygen (μmol kg^{-1}, log scale), and (d) fluorescence (log scale) for all CTD casts along the northern ($+$), central (circles), and southern ($\times$) transects carried out during UPSEN2 and ECOAO. (e) Differences between near-surface (s subscript) and bottom (b subscript) density are also shown as well as (f) the relationship between the

←

temperature and salinity contribution to these differences. Isolated dissolved oxygen values around or below 1.6 correspond to hypoxic conditions encountered at CTD 82 and on 16 Mar during two individual CTD casts at 14°N that are not part of the transect series. In (f), the dashed line indicates where temperature and salinity contributions are exactly opposite and compensate each other.
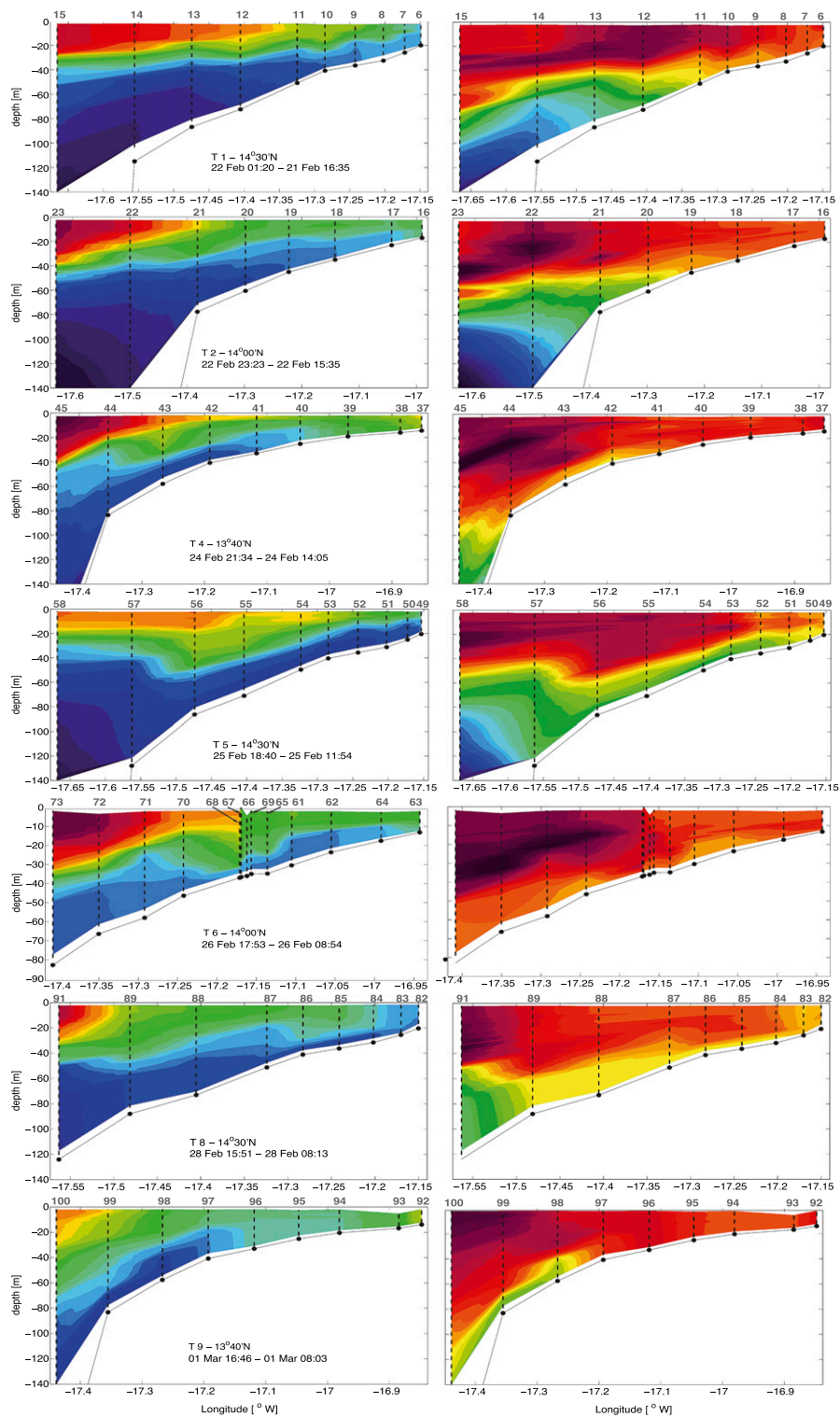
FIG. 6. (left) Temperature and (right) salinity CTD transects. Exact longitude range and maximum depth vary. CTD numbers are indicated in gray above the corresponding cast location (dashed line). Transect number, corresponding latitude, and time period are indicated in each temperature panel.
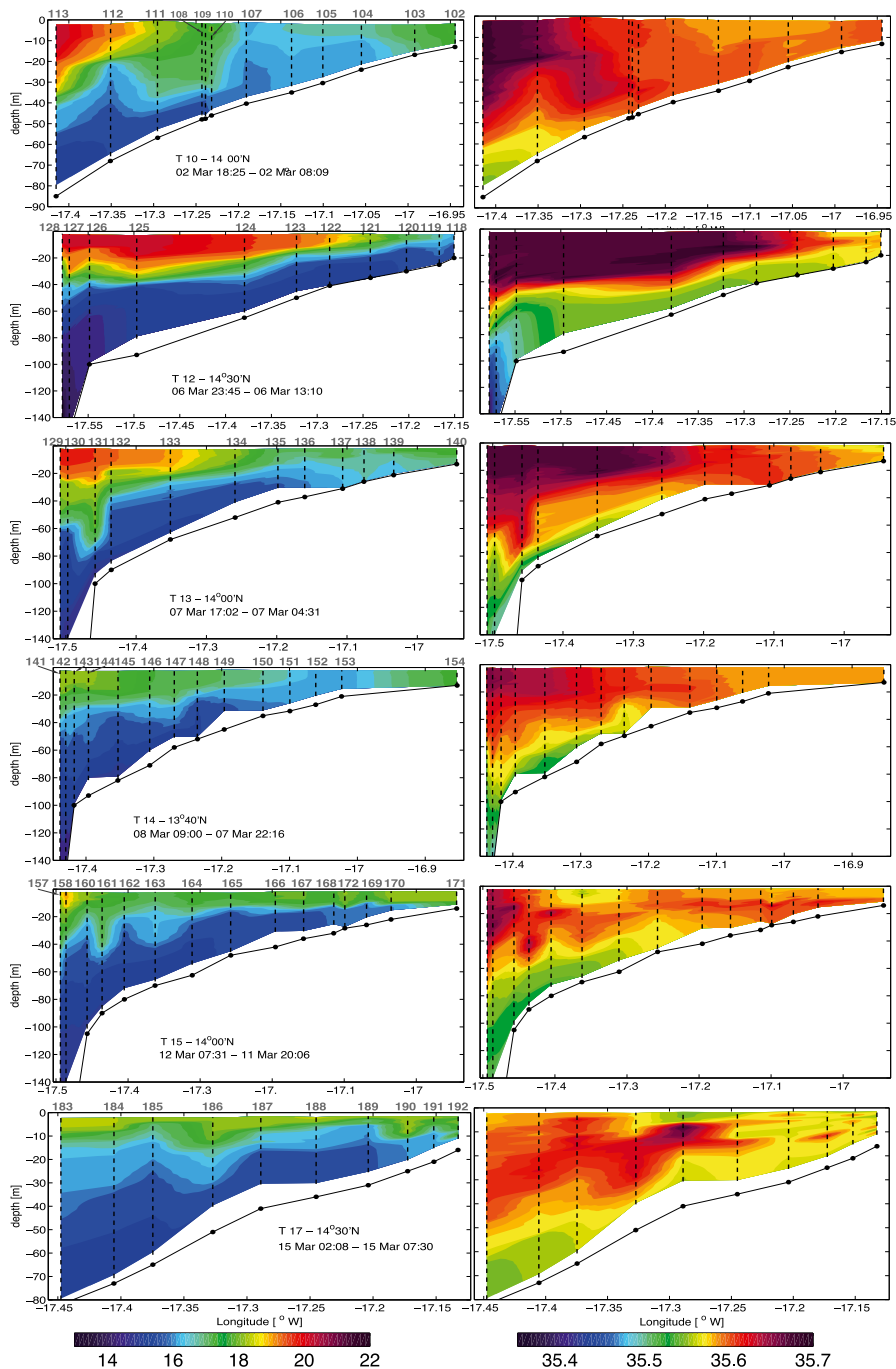
FIG. 7. (left) Temperature and (right) salinity CTD transects. Details as in Fig. 6.

are those where bottom water *T* and *S* properties are best preserved. Although this does not apply to T8 it confirms the visual impression from the SST images that the shelf is preferentially fed with slope waters in the northern SSUC. Many studies document the effect of capes and changes in shelf width on upwelling pathways and strength, which adds support to the visual impression

(Gan and Allen 2002; Pringle 2002; Pringle and Dever 2009; Gan et al. 2009; Crépon et al. 1984). Ongoing modeling work specific to the area is also supportive of this (Ndoye 2016).

The cross-shelf changes in tracer properties strongly depend on the tracer itself. Salinity contributes very little to density spatiotemporal variability (see Fig. 5f),

but its fluctuations over the shelf are nonetheless measurable and provide useful indications on mixing. Salinity and temperature experience marked relative changes between the shelf break and the 15-m isobath. The changes are most pronounced over the outer shelf for salinity with a tendency to saturation at about 35.6 psu for depths shallower than 40–50 m (Fig. 5b). The cross-shore structure is reversed for temperature with the most significant changes occurring at depths shallower than 30 m. However, the warming trend from deep to shallow parts of the shelf is ubiquitous. For dissolved oxygen, changes are very limited at depths greater than ~30 m and generally consist in a slight reduction from offshore to nearshore. For shallower depths, a large variability is found, particularly at the central and southern transects. Changes in fluorescence resemble those for oxygen, although they are less concentrated to the shallowest depths; for example, the outer shelf variability is much more pronounced.

Modification of bottom water biogeochemical properties when getting closer to shore goes in pair with a reduction in surface to bottom stratification (Figs. 5e,f), which occasionally vanishes inshore of the 30-m isobath. This points to the importance of vertical mixing as a process controlling the distribution of water column properties. Other processes shape the mean tracer distribution and in particular sources and sinks. We presume that biological activity is able to maintain sharp vertical contrasts in oxygen and fluorescence between the upper 20–40 m and the layer below and prevent mixing from significantly affecting the vertical distribution of these two tracers. For example, ventilation through mixing is unable to prevent hypoxia from developing toward the end of ECOAO during the relaxation period (see the three low dissolved oxygen outliers in Fig. 5c). This and other synoptic anoxic/hypoxic events are under investigation, similar to what is being done in other upwelling regions (Adams et al. 2013). Conversely, the absence of interior source/sink for temperature and salinity allows vertical mixing to have a significant impact on these fields.

Other aspects of the SSUC thermohaline structure suggest the importance of mixing. As mentioned in the introduction, the key dynamical feature of idealized upwelling models is their well-identifiable upwelling front, located where the main pycnocline outcrops and separates upwelling and nonupwelling waters. The complexity of the SSUC upwelling structure leads to equivocal situations regarding the definition/localization of the upwelling front and zone. In particular, the surface temperature and salinity across-shore gradients are frequently weak and diffuse, for example, 2°C over 25 km for T1, from CTD6 to CTD12. A notable

exception is found during T6 (14°N) where a 1.4°C change was observed over a horizontal distance of 250 m. Other exceptions are described in detail below as part of a submesoscale activity analysis.

More importantly, choosing a density/temperature value characteristic of the offshore pycnocline and following it toward the coast to its outcropping position does not reliably help define the location of the upwelling front, in contrast to, for example, what happens over the Oregon shelf (Austin and Barth 2002). The main reason for this is that considerable changes in stratification and thermohaline structure occur across the shelf, not just in the bottom layer as described above but also at middepth. Manifestations of intense mixing of thermocline waters include the presence of bulges of water in temperature classes that are almost unrepresented offshore (CTD43 in T4, CTD55–56 in T5, CTD70 in T6, CTD108–111 in T10, and CTD163 in T15).

In other words, except at the northern transects T1, T8, and T12 [which exhibit clear upwelling frontal structures as found, e.g., offshore of Oregon in Huyer et al. (2005)] and at the southern T14 [which resembles the idealized 2DV upwelling in Estrade et al. (2008) and Austin and Lentz (2002)], the exact location where upwelling is taking place is difficult to identify precisely. For example, T6 has a strong surface temperature gradient and an almost well-mixed water column at 17°10′W near CTD 66–69, but a significant amount of cold bottom water resides inshore of that location. A more dramatic example is obtained for T15 at the end of upwelling event UP1. On 12 March the upwelling front location at 14°N, determined as the place of zonal minimum SST (from MODIS SST in Fig. 2c or TSG data, not shown), sits around 17°25′W in 75-m water depth near CTD 163. On the other hand, a secondary SST minimum (see Fig. 2c) is found much closer to shore near M28, and the cold bottom water resides over most of the shelf, including at mooring M28 (see Fig. 8).

We attribute this complexity of the shelf thermohaline structure properties to intense vertical mixing. Although bottom friction may be also implicated, we present evidence that internal gravity waves breaking should play an important role as a source of mixing in section 4.

d. Midshelf dynamics

The description above can be complemented by and contrasted with the continuous current and temperature measurements available at 14°N about the 28-m isobath, although records cover a restricted period from 23 February to 12 or 15 March. In what follows, heat content is defined as $\int_{z_b}^{z_s} \rho C_p (T - T_m) \, dz$, where C_p is the heat capacity of water
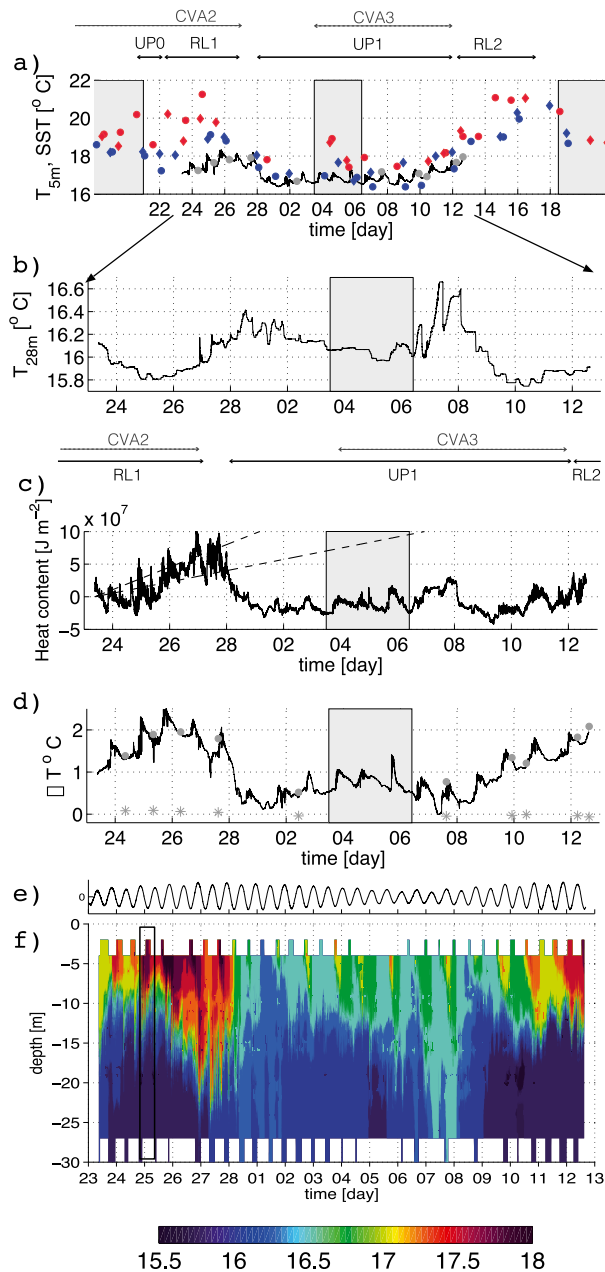
FIG. 8. Midshelf (M28) time series of (a) temperature at 5 m, (b) temperature at 28 m, (c) depth-integrated heat content (relative to the average over the entire deployment period see text for details), (d) near-surface (5 m) to bottom temperature difference, (e) bottom pressure anomaly at RDIE (panel range from −1 to +1 dbar), and (f) time–depth temperature diagram. The time range shown in (a) extends beyond the deployment period to represent MODIS SST before and after the experiment (blue/red symbols for nighttime/daytime scenes). The dashed lines in (c) represent heat content trends for a 1D ocean receiving a constant heat flux of 100 or 200 W m^{-2}. The frame delineated with black lines in (f) represent the time interval used to compute the typical energy and mixing potential of internal gravity waves in the midshelf (section 4).

taken equal to 3985 J kg^{-1} °C^{-1}, T_m is the mean vertical profile of temperature at M28 over the measurement period, and the integral goes from 5- to 27-m depth.

Heat content and stratification at M28 are mainly consistent with SST evolution there (or more broadly over the shelf); that is, they roughly follow the wind conditions. Heat content (Fig. 8c) undergoes a large increase from 25 to 27–28 February during RL1 and a rapid decrease on 28 February–1 March at the beginning of UP1. Changes before 25 February or after 1 March are comparatively modest in amplitude and rate, but an upward trend is noticeable from 2 to 8 March and 10 to 12 March, with a falloff between these two periods. Assuming that only air–sea exchanges contribute to the heat content increases during RL1 would imply a net air–sea heat flux of ≳ +200 W m^{-2} (see Fig. 8c), not inconsistent with climatological air–sea heat fluxes in late February/early March from COADS (140 W m^{-2}; Woodruff et al. 1998), OAFlux (105 W m^{-2}; Yu and Weller 2007), or CFSR reanalysis (120 W m^{-2}; Saha et al. 2010). During the UP1 onset phase a similar assumption would imply unrealistic heat losses of the order of −400 W m^{-2}, and lateral advection is thus necessarily implicated in the drop. The largest temperature changes are near the surface (Fig. 8f) where currents are about 3 times stronger than near the bottom (~25 vs 7–10 cm s^{-1}; see Fig. 9). This strongly suggests that a key term driving M28 heat content evolution in the beginning of UP1 is near-surface southward advection of cold water upwelled in the northern SSUC.

Daily and intradaily fluctuations are also present in the heat content signal particularly during the early (23–28 March) and to a lesser extent late (10–12 March) phases. The time scale of the fluctuations span a wide range of scales but periods of ~20 min or less dominate and reflect the importance of nonlinear internal waves (see next section).

Near-surface to bottom stratification evolution on synoptic time scales is similar to heat content, although, at the onset of UP1, it peaks about 1 day before on 26 March and drops more rapidly (Fig. 8d). We relate this to differences in the controlling processes. Indeed, the return of stronger winds enhances 3D turbulence levels and may erode stratification on a time scale of hours [2-hourly averaged winds reach 13 m s^{-1} on the evening of 27 February, which yields an increase in sustained maximum stress by 40% (100%) in comparison to 26 (25) February]. In contrast, changes in heat content should be more progressive because enhanced winds reduce air–sea heat fluxes by a few tens of watts per square meter only (given the range of wind fluctuations between RL1 and UP1), and changes in lateral

advection of cold waters should require one inertial period or more to be felt (Csanady 1982).

Nonzero stratification ($>0.5°C$ difference between top and bottom thermistors) is maintained during most of UP1. This is despite the fact that the mooring is located inshore of the main upwelling front during that period, as revealed in CTD transects T6 on 26 February, T10 on 2 March, and T13 on 7 March (see Figs. 6 and 7). There are only two brief moments when the water column is fully mixed or very near so: on 1 and 7 March. Winds measured by the ship at these times near M28 are the strongest observed during the entire period (Fig. 2d).

Bottom temperature evolution during the early UP1 period (between 26 February and 1 March) shows a pronounced increase ~0.5°C. This suggests that the initial response to increasing winds (enhanced vertical mixing) remains perceptible for 3–4 days at M28. Alternatively, warmer bottom waters may have been present north of M28 and the temperature evolution would simply result from their southward advection, but T5 and T8 temperature sections (Fig. 6) are not particularly supportive of this.

More generally, bottom temperature evolution at M28 illustrates the slow and complex response of bottom layer properties to the upwelling wind history; the coldest bottom temperatures coincide with the maximum relaxation during RL1 and also with the very end of UP1 and onset of RL2 (the return of bottom water as cold as that found on 25 February only occurs on 10 March). Conversely, the warmest temperatures are found after 8 days of sustained upwelling at the time when the coldest surface temperatures are recorded in the system (Fig. 2b). The long inertial time period (of the order of 2 days at the SSUC latitude) and, most importantly, the shelf width are two important factors that must contribute to the delays and decouplings between the onset of an upwelling-favorable wind event, cold water flowing over the shelf break, and that water reaching the M28 midshelf region. In turn, because the flushing of shelf bottom waters must take more time than, for example, relaxation RL1 lasts, the shelf thermohaline structure integrates the history of a succession of upwelling events (such as UP0 and UP1).

Midshelf alongshore currents (Fig. 9 at RDIE) essentially reflect the same RL1/UP1/RL2 succession of events with northward flow around 26 February and toward the end of the period (note that northward near-surface flows are only found in the core of RL2 with maximum intensity $0.1\,\mathrm{m\,s}^{-1}$). Southward flow prevails in between, with two surface peaks at approximately $0.4\,\mathrm{m\,s}^{-1}$ in conjunction with the well-mixed conditions on 1 and 7 March. Some important flow subtleties can also be noted.
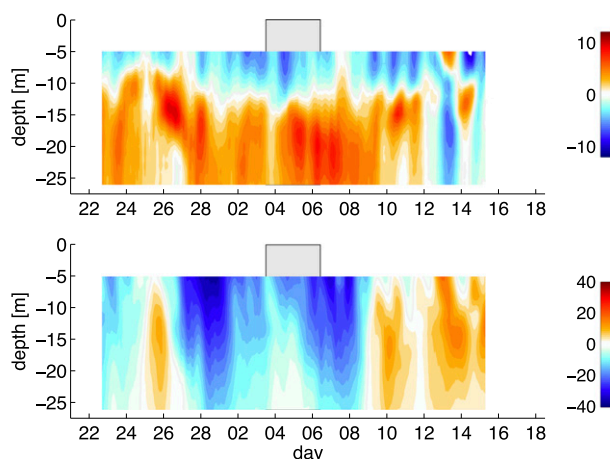

FIG. 9. (top) Midshelf (RDIE) time–depth diagram of detided zonal (i.e., cross shore u) and (bottom) meridional (i.e., alongshore) subinertial currents ($\mathrm{cm\,s}^{-1}$) over the entire deployment period. The white solid line represents the 0 isocontour. Note the different color scales for u and v. The gray rectangle corresponds to the time period when R/V *Antéa* was not at sea.

Most unexpectedly, a weak relaxation of the southward flow at RDIE stands out from 3 to 5 March. Alongshore currents do not reverse at RDIE, but they do at RDIW and AQDI, where the northward flow remains modest nonetheless, below $5\,\mathrm{cm\,s}^{-1}$ (not shown). Because the ship was not at sea during this time period, we lack contextual information to interpret these changes, but we note that wind intensity reduced slightly after 1 March (Fig. 2a), which may have been sufficient to trigger the southward flow relaxation. A similar explanation may be invoked to explain the timing of the alongshore current relaxation initiated around 9 March, that is, several days prior to the major RL2 wind drop but coincident with a limited wind reduction seen in DWS and ship atmospheric measurements (Figs. 2a,d). As noted previously, SST also suggests a RL2 initiation on 9 March, as opposed to 12 March when DWS winds strongly relax (see above). However, the wind drop around 8–9 March is limited (10% in meridional wind intensity at DWS; 30% in wind stress). Available satellite SST images offer additional insight into this early onset of RL2. In Fig. 3f, we have represented the position of the 20°C isocontour about two days prior to that scene at 2300 UTC 9 March. The change in contour location between 10 and 12 March suggests that flow relaxation/reversal over the midshelf during that period is part of a larger-scale tendency to northward advection. Whether the displacement of the slope mesoscale features is part of the response to a limited wind drop or is the cause of an early flow relaxation cannot be determined with the observations at our disposal. Below,

mesoscale activity will be more convincingly implicated as a direct cause of another synoptic flow fluctuation taking place over the shelf.

Cross-shore velocity evolutions have generally been more difficult to interpret than alongshore ones (Lentz and Chapman 2004). Subsurface cross-shore velocities are directed onshore during the entire UP1 period but also during RL1. During the first part of RL2, when RDIE is still moored, the current alternates between onshore and offshore with a period ~2 days suggestive of near-inertial oscillations (Millot and Crépon 1981). Cross-shore velocities in the surface boundary layer are essentially directed offshore. They are strongest during UP1 except for a short inversion to onshore coincident with the second time period when the water column is fully destratified. The first destratification episode on 1 March also coincides with reduced offshore flow near the surface. In both cases enhanced turbulent vertical diffusion of momentum at times of intense wind mixing are likely responsible for the anomalous onshore surface flow.

The largest cross-shore velocities are found at middepth on 26–27 February, that is, at a time when winds have started to increase moderately at DWS (wind evolution at M28 is less clear; see Figs. 2a,d) and the alongshore flow is not established to equatorward yet. The duration of this onshore pulse is too long to be consistent with a wind-induced inertial oscillation. An alternative explanation is suggested by the sequence of MODIS SST images for 24, 27, and 28 February (Figs. 3b,c, 4). These images offer a detailed view of the mesoscale activity and its evolution during that period. On 27–28 February, a warm MC meander that will subsequently form CVA-3 impinges on the shelf with its edge reaching the 30-m isobath. Comparison with the image for 24 February indicates that a rapid displacement of the meander crest toward the northeast (i.e., toward the mooring area) has taken place over 2–3 days. Concomitantly, the cold upwelling tongue undergoes a noticeable shoreward displacement (followed by a rapid offshore retreat). On 27 February, it occupies a zone inshore of M28 at 14°N (Fig. 4). The existence of a short-lasting onshore advection episode is also consistent with temperature observations at M28, where a substantial lateral flux contribution is required to explain the heat content increase around that day (Fig. 8c).

Because R/V *Antéa* steamed multiple times across the mid- and outer shelf in the latitude range 14°–14°10′N between 0300 UTC 26 February and 0030 UTC 28 February, additional observations are available to support the existence of a shelfwide event of onshore flow driven by mesoscale activity. A cross section of (u, v) velocities is obtained by averaging the ship ADCP measurements made during these transects. Data are binned using the native resolution of the ADCP in the vertical (8-m bins; the uppermost one being centered at -19 m) and a 0.025° mesh size in longitude. The ADCP configuration used 5-min ensemble averaging. All the ensembles for a given transect falling into one 0.025° longitude bin are preaveraged and contribute for only one observation. We did not try to weight the transects so as to minimize the influence of tidal currents [e.g., as done in Avicola et al. (2007)], but we have verified that tidal phases are such that substantial canceling is happening in the averaging (which is only important for u given the shape of tidal ellipses; not shown). The result is shown in Figs. 4a and 4b and allows us to place the mooring observations around 27 February in a broader across-shore perspective. During this period subsurface currents over most of the shelf are toward the northeast. Onshore velocities reach $20 \, \mathrm{cm \, s^{-1}}$ over the outer shelf with a maximum positioned at middepth. Onshore velocities remain $\sim 10 \, \mathrm{cm \, s^{-1}}$ as close to shore as the ship ADCP can measure. Closer to shore RDIW and RDIE zonal velocities are also around $10 \, \mathrm{cm \, s^{-1}}$. Inspection of all available ship ADCP transects near 14°N confirm the unusual intensity of this onshore flow. Intense poleward currents, as those depicted in Fig. 4b, are more commonly observed, although they are generally confined to the slope and outer shelf area.

SST images during the UPSEN2–ECOAO (and at other times) clearly show the frequent incursion of MC mesoscale meanders and eddies onto the shelf. These are presumably the manifestations of instability modes for the system formed by the poleward current and the equatorward upwelling flow. Based on the discussion above, we see the episode of onshore flow on 26–27 February as related to such a mesoscale event. The unstable behavior of a shelf/slope current system has recently been studied in the downwelling case (Wang and Jordi 2011). Our observational results highlight the need to perform a similar study in the context of upwelling systems. This would help explore and clarify the interactions between the shelf upwelling jet and the slope current, the influence of the wind in modulating these interactions, and, most importantly, the conditions under which mesoscale perturbations penetrate deeply into the shelf.

e. Flow parameters and regime

Several important flow characteristics can be derived from the observations and analyses presented in the previous section, with the objective to compare the SSUC to other upwelling regions.

From Fig. 5e, the Brunt–Väisälä frequency can be computed at every CTD station. Ignoring a few outliers, we find relatively uniform values for $N \approx 10^{-2} \, \mathrm{s^{-1}}$. It

yields deformation radius values ranging from $\approx 8\,km$ at midshelf to $27\,km$ at the shelf break, that is, on the higher end of what is typically found in upwellings. This is mainly because the Coriolis parameter is small ($f = 3.6 \times 10^{-5}\,s^{-1}$ at $14°30'N$). The topographic slope along all three transects is also quite uniform $\alpha \approx 2 \times 10^{-3}$. The resulting slope Burger number $B = (\alpha N)/f$ is around 0.5. In a steady 2D upwelling, the way the return onshore flow balancing offshore Ekman transport is achieved depends on B (Lentz and Chapman 2004). A value of B smaller (greater) than 1 implies that the wind stress is balanced by bottom friction (nonlinear across-shelf flux of alongshore momentum), so the return flow is concentrated in the bottom boundary layer (distributed in the water column below the surface boundary layer); $B = 0.5$ suggests the importance of frictional forces in the alongshore momentum balance but is comparable to values found offshore of Oregon and northern California, where both the topographic slope and Coriolis frequency are larger (Lentz and Chapman 2004). The prominence of the cold bottom layer rising up the shelf in most T–S transects (Figs. 6, 7) is qualitatively consistent with this.

Geostrophy is an important force balance that the nontidal part of the flow should approximately satisfy. Tidally filtered RDIE currents at M28 described above exhibit substantial fluctuations on time scales of 1 day or less, particularly in the alongshore direction (Fig. 9). This suggests that deviations from geostrophy are important, and the subinertial flow is characterized by Rossby numbers that are not negligibly small compared to 1. Because wind fluctuations do not conclusively explain several rapid flow changes, we tend to see this as a manifestation of the submesoscale dynamics in the upwelling zone.

Submesoscale turbulence consists of fronts, small eddies, and filaments with typical horizontal scales $\lesssim R_d$ (where R_d is the first deformation radius) and a strong tendency to near-surface intensification. Key processes for submesoscale generation are (Capet et al. 2008d) (i) straining/frontogenesis by mesoscale structures, which intensifies preexisting buoyancy contrasts and leads to fronts whose vertical scale is typically that of the mesoscale, and (ii) straining/frontogenesis by finescale parallel flow instabilities, which distorts mesoscale buoyancy gradients and produces submesoscale flows whose vertical scale can be much smaller than that of the mesoscale. An archetypal example of point ii is mixed layer baroclinic instability, which generates submesoscale flow fluctuations approximately confined into the mixed layer (Boccaletti et al. 2007; Capet et al. 2008d). In their most extreme manifestations, contrasts across submesoscale fronts can reach several degrees over lateral scales of 50–100 m. Such contrasts are the consequence of intense straining in situations where diffusion is weak.

Upwelling dynamics are well known to induce intense submesoscale frontal activity, but some precision is in order to connect with our SSUC study. Submesoscale fronts are ubiquitous in the offshore coastal transition zone where cold upwelled and warm offshore waters are being stirred (Flament et al. 1985; Capet et al. 2008c; Pallàs-Sanz et al. 2010). Our study is concerned with shelf dynamics where the interaction between cold upwelling and warmer offshore waters is strongly constrained by topography, friction, and inertia–gravity wave (IGW) breaking. A numerical investigation of the northern Argentinian shelf dynamics indicates that the submesoscale is strongly damped in water depths shallower than $\sim 50\,m$ (Capet et al. 2008a) and the same should apply to the SSUC; hence, we expect limited submesoscale turbulence over the inner- and midshelf. On the other hand, the upwelling front is frequently located over the outer shelf where it can be subjected to straining by CVAs so it is a priori conducive to the formation of submesoscale features.

To explore this possibility, we use TSG temperatures from multiple across-shelf transects conducted between 9 and 10 March at $14°$ and $14°05'N$, a subset of which is presented in Fig. 10. Temperature contrasts across the upwelling front are clearly modulated at scales of a few hours and less than $10\,km$ in the alongshore direction, that is, at submesoscale. Temperature differences of $\sim 1°$–$2°C$ over 100–200 m are found (two bottom panels in Fig. 10) and must reflect localized straining and frontogenesis. At earlier times, temperature changes are much smoother. A process that might be responsible for such modulations would be the submesoscale destabilization of the upwelling front with alternating frontogenesis and frontolysis in relation to crests and troughs of unstable waves (Spall 1997). Some of the satellite images are consistent with this (Fig. 3b; see the two filamentary regions around $13°15'$ and $13°45'N$, $17°15'W$), but submesoscale distortions of the upwelling front are modest and infrequent compared to observations for other regions [see Fig. 3 and compare it with Fig. 3c in Capet et al. (2008a) and Fig. 16 in Capet et al (2008d)]. Over most images, front sharpness has evident alongfront variations, but these variations are more commonly at the mesoscale (Figs. 3a,c,e and 4, top) in relation with straining by CVAs; hence, process i seems more important than process ii. This may be otherwise during periods where stronger winds and possibly destabilizing air–sea heat fluxes lead to deeper mixed layers and thus more energetic submesoscale instabilities (Fox-Kemper et al. 2008). Note that we see no

signs of subduction/upwelling at the upwelling front, but we lack high-resolution subsurface measurements that would allow us to observe their finescale signature, for example, on biogeochemical tracers (Evans et al. 2015). Note also that preferential but intermittent internal wave dissipation/mixing in the vicinity of the upwelling front could well contribute to the alongfront modulations of its sharpness (see next section).

4. The SSUC internal wave field

Internal gravity waves are well known contributors to mixing in the coastal ocean. The accepted view is that internal tides generated at the shelf break tend to evolve nonlinearly and give rise to shorter-scale internal waves as they propagate nearshore. Steepening and breaking (Moum et al. 2007, 2003; Lamb 2014) is inherent to the propagation toward shallower waters, but the subinertial environment can also enhance dissipation, for example, through mutually reinforcing shears as found by Avicola et al. (2007). This latter study indicates that, over the Oregon shelf, internal wave breaking has a modest impact on vertical fluxes of tracers, a conclusion also reached by Schafstall et al. (2010) for the central Mauritania outer shelf region, just a few degrees north of the SSUC.

Isolated satellite measurements suggest that the SSUC is also subjected to IGW wave activity (e.g., Jackson and Apel 2009). In this section, we describe circumstantial evidence that SSUC IGW activity was ubiquitous during UPSEN2 and ECOAO and that its intensity was at times very strong. Because we did not have any microstructure sensor onboard, no direct local dissipation estimates are available. On the other hand, our observations point to the importance of mixing not only near the bottom where frictional effects may be implicated, but also in the intermediate part of the water column where significant water mass transformation is revealed by several CTD casts (Figs. 6 and 7; e.g., CTDs 55–56 in T5; 108–111 in T10). In addition, midshelf observations from moored instruments are used to estimate the energy associated with wave packets, which seems enough to influence the evolution of the upwelling front region.

a. Circumstantial evidence

R/V *Antéa* is equipped with a four-frequency EK60 echosounder (see section 2). Inspection of all available echograms indicates ubiquitous nonlinear internal wave activity over the southern Senegal shelf. During UPSEN2, these waves manifest themselves as depressions of the main thermocline located in the vertical at about 1/3 of the water depth. Maximum crest to trough amplitude frequently reach 40 m or more over the outer shelf (see Fig. 11). Short internal waves (wavelengths of a few
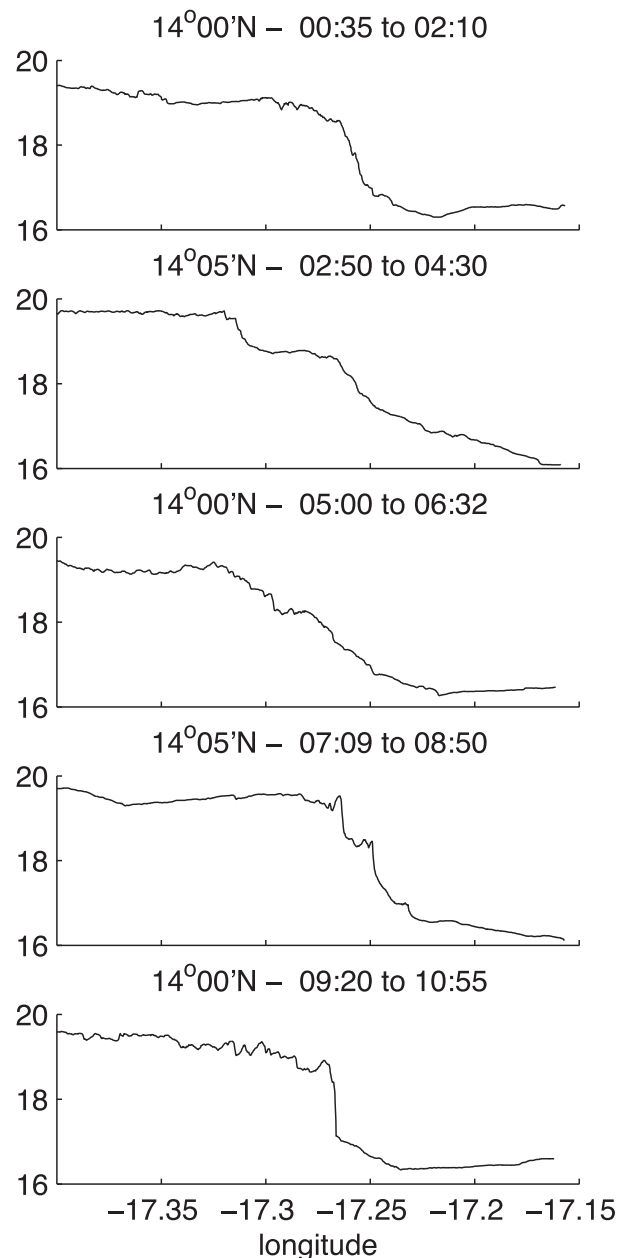

FIG. 10. Across-shore TSG temperature for five transects carried out on 9 Mar 2013 over time intervals that are specified above each panel, along with the exact latitude of the transect (14°00′ or 14°05′N). Note the rapid changes in temperature distribution with time and latitude.

hundred meters) are embedded into longer waves (wavelengths around 10 km), as in situations where internal tides undergo fission (Gerkema 1996; Li and Farmer 2011).

Beside visual resemblance between the patterns exhibited in Fig. 11 and commonly observed internal gravity waves, both yoyo CTDs and ScanFish observations at constant depth confirm that echograms reflect

displacements of the thermocline associated with time periods of a few minutes and amplitudes of tens of meters. Several yoyo CTDs were performed in the hope that they would help quantify mixing intensity. One took place on 25 February at 14°N, 17°20′W in about 60-m water depth as the leading edge of an internal tidal wave passed that location (Fig. 12a). A Thorpe-scale analysis is performed on the 17 downcast profiles, following Thompson et al. (2007). Note that Thorpe-scale analysis is only valid when horizontal density gradients can be neglected (Dillon 1982). TSG data obtained immediately prior to the yoyo station provide a useful estimate of the horizontal density gradients in the station vicinity. The density gradient is smooth and relatively constant in the area with a typical maximum value for $(g/\rho_0)\partial_x\rho$ around $2.5 \times 10^{-6}\,\text{s}^{-2}$. Thorpe overturns with N^2 lower than twice this value will be put aside. Dominant vertical gradients in salinity are by far those associated with spikes induced by thermal lag in the conductivity sensor. On the other hand, salinity has a minor effect on density gradients, both horizontally and vertically with a salinity range whose amplitude is systematically below 0.2–0.25 psu over the entire shelf, that is, equivalent to ~1°C in its effects on density (see Fig. 5f). By comparison, temperature gradients are 4–5 times stronger. As in Alford and Pinkel (2000), we therefore compute Thorpe displacements and overturn scales based on temperature alone (see Figs. 12b–d). Finally, note that estimates of vertical diffusivity K_v are computed assuming constant mixing efficiency $\gamma = 0.2$.

The weakly stratified upper layer is where the largest Thorpe displacements and dissipations are found (as in Moum et al. 2007) with values occasionally reaching $10^{-5}\,\text{W kg}^{-1}$. Vertical diffusivity values are also large, in the range 10^{-3}–$10^{-2}\,\text{m}^2\,\text{s}^{-1}$. Weaker dissipation maxima ~$10^{-7}\,\text{W kg}^{-1}$ are found in the lower half of the water column at that particular station. Middepth ε one order of magnitude larger are obtained for one profile (not shown) carried out in the vicinity of CTD 89 (transect T8) where both temperature and salinity show conspicuous signs of interior mixing (see Fig. 6). Overall, interior K_v values are frequently in the range 5×10^{-5}–$5 \times 10^{-3}\,\text{m}^2\,\text{s}^{-1}$, but they are most often associated with overturns at the margin of detectability with standard CTD measurements. More sophisticated methods will be needed to characterize and quantify the intensity of localized mixing episodes induced by internal gravity waves and their relationship with the shelf environment (Walter et al. 2014; Palmer et al. 2015).

b. Midshelf IGWs and their effect on the upwelling front

A different approach to quantify the effect of IGW mixing relies on bulk estimates of IGW dissipated power
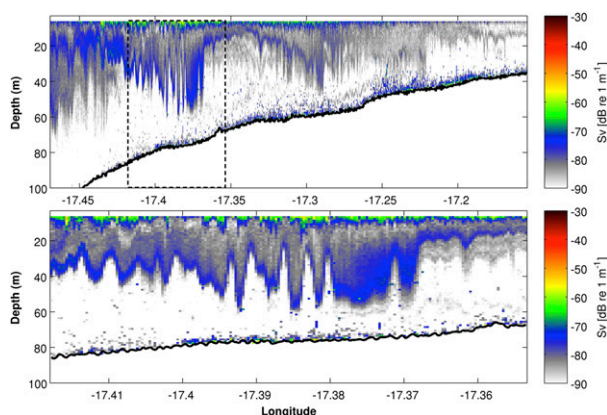

FIG. 11. (top) 70-kHz echograms obtained on 23 Feb between 0222 and 0600 UTC while R/V *Antéa* steamed eastward at a nearly constant speed ~5 kt. Moderate backscatter levels in blue indicate the position of sharp density gradients. They exhibit oscillations with wavelengths of the order of a few hundred meters embedded into longer internal tides (two wavelengths around 10 km are visible with troughs at 17.47°, 17.37°, and 17.29°W and crests at 17.45° and 17.34°W). (bottom) Zoom over the time subinterval 0258 to 0343 UTC indicated by a rectangle in the top panel. Bottom depth measured by the ship ADCP is indicated by a thick black line. Data treatment is performed using the ECHOPEN software (http://www.france-nord.ird.fr/les-ressources/outils-informatiques).

over portions of the shelf (Jeans and Sherwin 2001). Depending on the SSUC thermohaline structure, a given fraction of the energy converted to baroclinic tides at the shelf break is able to propagate nearshore to the midshelf area. Sampling intervals of two moored ADCPs (2 min for RDIW and RDIE) and thermistors mounted on M28 (1 min) are adequate to resolve IGW activity when it is present. For example, the signature of wave packets is visible at M28 in temperature, mainly before 28 February and to a lesser extent after 10 March (Fig. 8).

In the remainder of the section, mooring data are used to compute 1) internal gravity wave energy at that location and, under some assumptions, 2) how much mixing can be achieved in the midshelf area where that energy can dissipate.

Given the observations at hand, we choose to estimate the IGW energy flux F^w passing through M28 as $c_g(\text{EKE}^w + \text{APE}^w)$, where c_g is the speed at which wave trains propagate in the area and EKE^w (APE^w) is the depth-integrated kinetic (available potential) energy associated with IGWs. This requires the definition of a low-pass operator $\overline{\cdot}$ such that high-pass deviations (denoted with a prime) adequately capture the flow and thermohaline fluctuations corresponding to IGW activity. We use a running mean with flat averaging over time intervals of duration T_{lf} longer than the internal wave period for $\overline{\cdot}$.

The term APE^w is quantified using the approach valid for arbitrary stratifications detailed in Holliday and
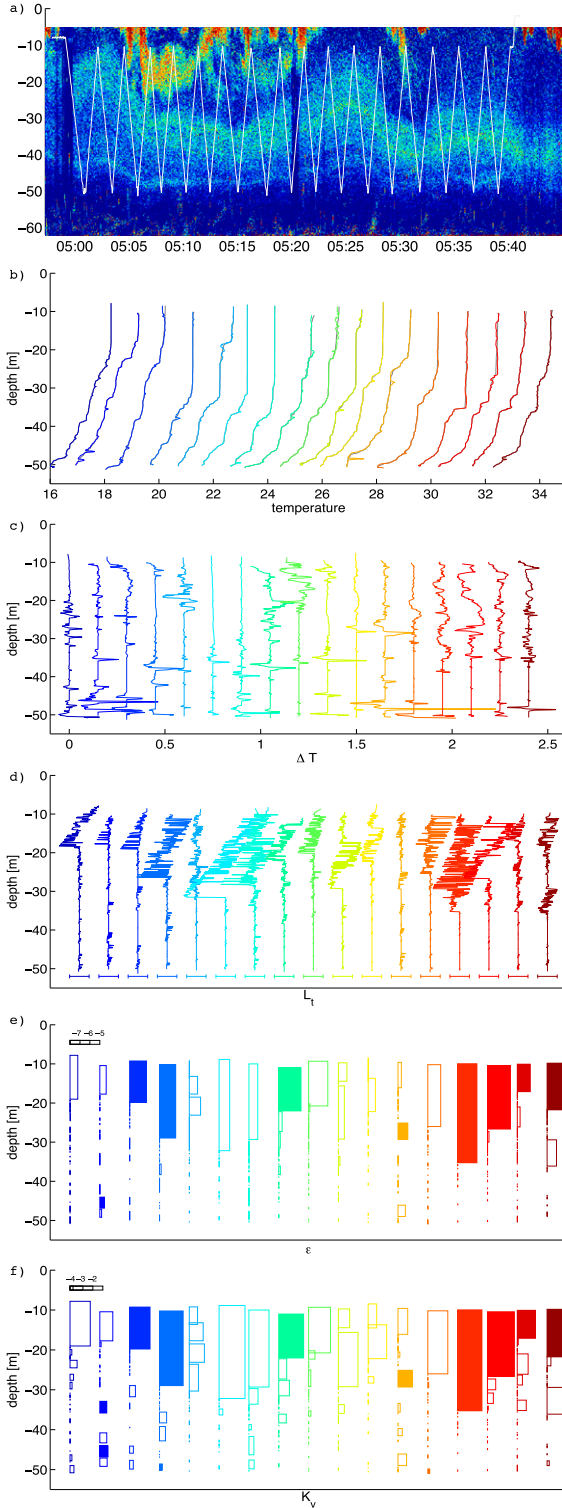
FIG. 12. (a) 70-kHz raw echograms obtained on 25 Feb between 0500 and 0540 UTC while R/V *Antéa* was in station around 14°N, 17°20′W. The position of the CTD is superimposed as white segments forming a zig–zag pattern. (b) Profiles of temperature (with a 1.5° shift between them), (c) anomaly between the measured and stable reordered temperature profile (0.15°C shift), (d) Thorpe

McIntyre (1981) [see also Roullet and Klein (2009) and Kang and Fringer (2010)]:

$$\mathrm{APE}^w(t) = \int_{-H}^{0} \left\{ \int_{\overline{z}_r[\rho(z,t),t]}^{z} g[\rho - \overline{\rho}_r(z',t)]\,dz' \right\} dz, \quad (1)$$

where $\overline{\rho}_r(z, t)$ is the density profile of the reference state, and $\overline{z}_r(\rho)$ is its bijection, that is, the equilibrium depth of a parcel of density ρ. Density reference states are determined by reordering density observations over overlapping time intervals of duration T_{lf}. Each resulting reference state is then used to compute $\mathrm{APE}^w(t)$ over a time subinterval of size T_{sub} smaller than T_{lf} (to limit edge effects). Choosing T_{lf} in the range [0.5–3]h and T_{sub} from ⅓ to $1 \times T_{\mathrm{lf}}$ does not reveal important sensitivities of either APE^w or EKE^w estimates. We present results for $T_{\mathrm{lf}} = \mathrm{T}$ 30 min and $T_{\mathrm{sub}} = 15$ min.

The term EKE^w is quantified as

$$\mathrm{EKE}^w(t) = \frac{1}{2}\rho \int_{-H}^{0} (u'^2 + v'^2 + w'^2)\,dz - \mathrm{EKE}^{\mathrm{bg}}. \quad (2)$$

In this definition $\mathrm{EKE}^{\mathrm{bg}}$ represents the nonzero background value of the high-pass eddy kinetic energy found even during the period when the mooring is located inshore of the upwelling front. Fast motions may be due to other processes than internal gravity waves that we wish to exclude from the analysis, including instrument noise. Based on Fig. 14 (shown below), a conservative value for $\mathrm{EKE}^{\mathrm{bg}}$ is 24 J m^{-2}. In practice, vertical integration ranges for APE^w and EKE^w are restricted to where valid observations are available (see section 2).

To determine c_g, we estimate the delay between the arrival of particularly identifiable wave trains at RDIW, M28, and RDIE. This method has inherent uncertainties because the wave trains can be significantly modified, particularly between RDIW and RDIE, which are separated by ~1 nm; c_g values are in the range 0.18–0.30 m s^{-1}. For the wave train shown in Fig. 13, the estimation is quite accurate between M28 and RDIE (despite inconsistencies prior to the arrival of the main wave packet; see Fig. 13). It yields $c_g = 0.25$ m s^{-1}, a central value we retain for further use below. Incidentally, Fig. 13

←

displacement (m; the extremities of the segments below each profile indicate ±5 m), (e) energy dissipation (W kg^{-1}; log scale), and (f) turbulent diffusivity (m^2 s^{-1}; log scale). In (e) [(f)] values below 10^{-8} (5×10^{-5}) are not shown. Bars corresponding to overturns with temperature amplitudes larger than 0.05°C and $N^2 > 5 \times 10^{-6}$ s^{-2} are filled. The latter condition only excludes the minor overturn of cast eight centered on 30-m depth.
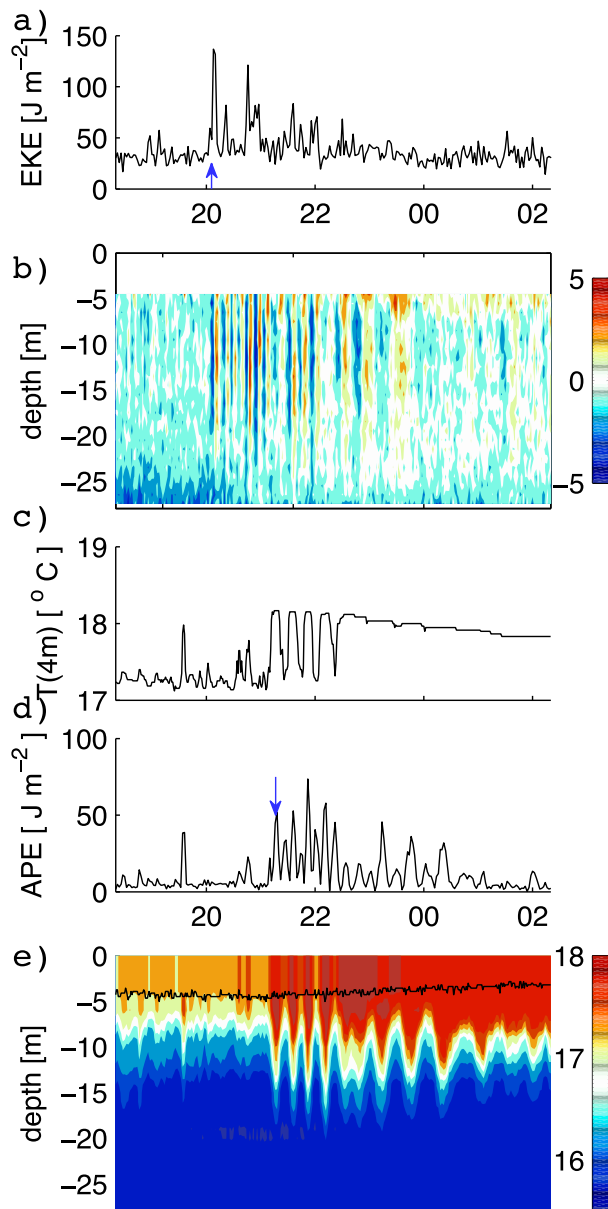
FIG. 13. Time series of (a) vertically integrated eddy kinetic energy and (b) vertical velocity at RDIW; (c) 4-m depth temperature, (d) vertically integrated available potential energy, and (e) time–depth temperature diagram at M28. Time period is 1820 UTC 24 Feb to 0220 UTC 25 Feb, that is, during the active period of IGW activity studied in section 4. The depth of the shallowest thermistor is indicated with a black solid line in (e) (its mean depth over the period is 3.83 m. Blue arrows in (a) and (d) indicate the times of wave packet arrival used to estimate c_g (see text for details). The x-axis scale is identical in all panels.

also suggests the role that wave trains can play in mixing the near-surface heat accumulated in the warm diurnal layer when winds are weak as on 24 February (see the abrupt change in temperature at 4-m depth as waves reach

M28; similar evening drops in temperature synchronized with wave packet arrivals are observed on 23 and 25 February).

The values of APE^w at M28 and $EKE^w + EKE^{bg}$ at RDIW are presented in Fig. 14 over the entire period of deployments. Several wave packets have clear signatures, both instantaneous and on average over a M_2 period, particularly during RL1. For example, between 2000 UTC 24 February and 2030 UTC 25 February (Fig. 13), the mean energy at the moorings is $20 \, \mathrm{J \, m^{-2}}$, with a near-exact equipartition between potential and kinetic wave energy. This yields $F^w = 5 \, \mathrm{W \, m^{-1}}$, in line with mid- and inner-shelf values found off southern California (Lucas et al. 2011b) and Oregon (Torgrimson and Hickey 1979).

An interesting point of comparison can be obtained by computing the speed at which the internal wave energy can fully mix the water column in the offshore vicinity of the upwelling front and thus lead to its westward migration. During periods where the upwelling front is near M28 on its inshore side, the IGW flux passing at M28 will be progressively dissipated in a region of across-shore size L_x between M28 and the upwelling front, inshore of which internal waves cannot exist because there is no stratification to support them. A fraction γ of this dissipation will be available for mixing. The typical speed c^w_{front} at which the upwelling front can be displaced seaward by IGW dissipation is

$$c^w_{\mathrm{front}} = L_x \frac{\gamma F^w}{\displaystyle\int_{L_x} E^{\mathrm{mix}}(x) \, dx},$$

where $E^{\mathrm{mix}}(x)$ is the potential energy excess resulting from the homogenization of the stratification present at cross-shore location x in the hours preceding the arrival of a given wave packet. The integral concerns the L_x-wide region between M28 and the upwelling front. Assuming that E^{mix} is constant over that restricted area yields $c^w_{\mathrm{front}} = \gamma F^w / E^{\mathrm{mix}}(\mathrm{M28})$, independent of L_x; E^{mix} values computed at M28 are in the range 300 to $450 \, \mathrm{J \, m^{-2}}$ and close to $350 \, \mathrm{J \, m^{-2}}$ on the afternoon of 24 February. Assuming a mixing efficiency $\gamma = 0.2$ (Osborn 1980) leads to $c^w_{\mathrm{front}} \approx 250 \, \mathrm{m \, day^{-1}}$. This is modest and would translate into a 10 km offshore displacement over the duration of our field experiments. There are, however, several sources of uncertainties in the calculation, for example, in the mixing efficiency (Walter et al. 2014). Perhaps most importantly, the internal wave field energy is estimated at M28 where it has already been strongly attenuated (through interactions with the bottom and also heterogeneities of the density field). An estimation performed farther offshore would
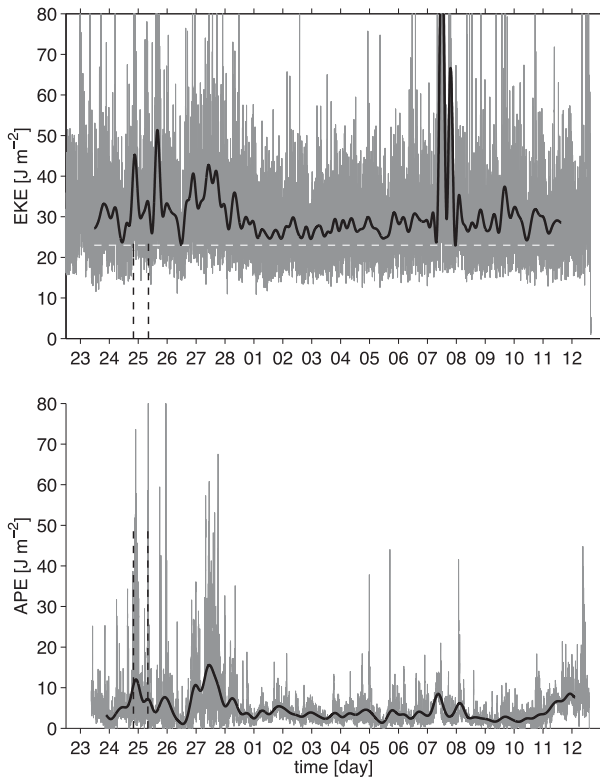
FIG. 14. Time series of (top) eddy kinetic energy (EKE^w) plus its background level EKE^{bg} (horizontal white dashed line) and (bottom) available potential energy (APE^w) at M28. In both cases unfiltered (thin gray) and low-passed (Lanczos filter with cutoff at the M_2 frequency; black) signals are shown. Lower signal to noise ratio for EKE^w computed from ADCP observations is evident. The time interval 2000 UTC 24 Feb–2030 UTC 25 Feb chosen to estimate IGW mixing in section 4 is delineated by black dashed vertical lines.

result in larger F^w. On the other hand, $(1/L_x)\int_{L_x} E^{mix}\,dx$ would also be larger, so the outcome in terms of displacement speed c^w_{front} is uncertain. During an earlier field experiment in March 2012 where only moored ADCP measurements are available midshelf EKE^w, values of up to 30 J m^{-2} over a tidal period are found, while E^{mix} is only marginally larger (UPSEN; P. Estrade et al. 2016, unpublished manuscript), so c^w_{front} may reach 1 km day^{-1} on some occasions.

The complications and uncertainties associated with the alongshore dimension should also be kept in mind. The manifestations of mixing observed at the central and southern transects result from a history of mixing along the 3D path of water parcels. These manifestations tend to be dominated by the presence of bulges of mixed water located immediately offshore of regions of strong SST gradients. This is particularly evident where upwelled and warm waters of offshore origin are in contact over the shelf (T6, T10, and to a lesser extent

T4). The pathway of the modified subsurface waters making up these bulges cannot be determined precisely. But general considerations on frontal dynamics suggest that this water may remain trapped in the frontal region while drifting alongshore and undergoing IGW mixing. Under upwelling-favorable condition slope waters should preferentially be upwelled onto the shelf in the northern SSUC (Crépon et al. 1984; Ndoye et al. 2014) and subsequently drift equatorward (S. Ndoye et al. 2016, manuscript submitted to *Geophys. Res. Lett.*), hence the weakest bottom salinities over the shelf found for T1 and T5 and the weaker signs of IGW mixing there. With these considerations in mind, the limitations of our Eulerian estimate of IGW mixing potential at one particular location of the midshelf at 14°N are evident. IGW trains with the largest amplitude (~70 m) found during UPSEN2–ECOAO were observed on 28 February around CTD 89 (T8) in 90–100-m water depth. The signature of mixing is noticeable on CTD profiles performed in the area shortly after their sight (not shown). Whether elevated northern IGW activity contributes to the formation of transformed waters present on 2 March in the frontal area near CTD 108–111 (approximately 50 km to the south) cannot be determined but is consistent with ship ADCP measurements showing southward velocities over the shelf with velocities between 15 and 30 cm s^{-1}.

Longer-term observations at different locations over the shelf would be needed to clarify these issues. They would also allow us to explore the possible relationship between the amplitude of the wave packets and the spring–neap cycle. Present observations are ambiguous on this matter because the only neap tide period during the field experiment (centered on 7 March; see Fig. 8e) coincided approximately with the lowest midshelf stratification.

5. Conclusions

The present study is the first analysis of comprehensive physical in situ observations carried out in the SSUC. A number of findings complement and qualify previously known aspects of the SSUC dynamics.

The manner in which the upwelling zone and frontal positions are established has previously been seen in a 2D, vertical subinertial framework, as a consequence of the shutdown of surface Ekman transport in shallow waters. Essential to the conceptual model is the assumption that momentum is sufficiently well mixed inshore of the upwelling zone so that wind and bottom friction equilibrate without involving the Coriolis force (Ekman 1905). In this conceptual model, wind strength can modulate the position of the front (Estrade et al.

2008) by affecting surface (Lentz 1992) and, more indirectly, bottom turbulence intensity. Overall, our continuous observations reveal that the water column is rarely destratified and momentum is not well mixed even tens of kilometers inshore of the upwelling front. Although the model may retain some validity at other times or on different time scales, other processes may be more important for the upwelling variability over periods of days to weeks and, in particular, where subsurface water is upwelled, which parts of the shelf it enriches, and how the enriched area and its frontal edge may migrate across shore with time. In light of our analyses and findings, we hypothesize that two key processes (with possible interplay between them) also play a systemic role in the functioning of the southern Senegal shelf upwelling.

First, the upwelling tongue and its frontal separation from the offshore waters are subjected to mesoscale disturbances, which bring important non-2D effects. In the northern part of the system, a recurrent expression of mesoscale turbulence during UPSEN2–ECOAO was through 50–100-km anticyclones that remained quasi stationary for one to a few weeks offshore of the Cape Verde Peninsula. These Cape Verde anticyclones (CVAs) develop as meanders of the system formed by the Mauritanian Current and shelf upwelling currents that abut onto the Cape Verde Peninsula. CVAs have a clear influence on the shelf upwelling structure. They tend to confine the upwelling tongue nearshore in the northern SSUC and promote offshore export of recent upwelled water near 14°N. A better understanding of the unstable behavior of the shelf/slope current system would be useful and, in particular, (i) the conditions under which they can influence the shallow parts of the shelf [as around 27 February and possibly at the beginning of the second relaxation (RL2) between 9 and 12 March] and (ii) their preferential evolution sequences and their relation to environmental conditions, including wind fluctuations. Our observations are broadly consistent with the fact that shelf current reversals associated with wind relaxations contributed to the flushing of CVA1 and CVA2 away from Cape Verde, although these two structures were strongly diminished in strength at the time of flushing.

Another possibly important mechanism affecting the distribution of upwelling and the evolution of the frontal zone is mixing by internal tide dissipation over the shelf. To frame the issue, we find it useful to examine a fast upwelling limit case that would be exemplified by central California, where w^{up} is classically tens of meters per day (Capet et al. 2004). In such a situation the upwelling process may be adequately pictured as adiabatic upward advection while vertical mixing is ignored because it

merely performs the inescapable incorporation of upwelling water into the mixed layer. This incorporation is tightly slaved to the vertical advection itself. Complexity in vertical mixing, resulting from external processes (e.g., internal tide dissipation) or from heterogeneities directly associated with the upwelling dynamics (e.g., nearshore wind dropoff) can only produce minute changes to where and when upwelling water is entrained into the surface mixed layer. External sources of mixing also have little time to act on upwelling water because w^{up} is large.

A radically different type of surface layer enrichment regime has been identified over some shelves where patchy episodes of vertical mixing triggered by inertia–gravity wave activity is the key process that incorporates subsurface water into the euphotic layer while unspecified adiabatic processes are in charge of renewing the pool of bottom water awaiting mixing with surface waters (Sharples et al. 2007; Williams et al. 2013; Tweddle et al. 2013) [see also Lucas et al. (2011b) in which southern California internal tides are shown to be responsible for the across-shelf replenishing flux of nutrients].

The SSUC situation uncovered during UPSEN2–ECOAO may represent an intermediate situation where partial decoupling between upwelling-driven vertical advection and mixing leads to incorporation of bottom water into the surface layer through multiple sporadic mixing episodes. In the SSUC, we expect the onshore flow to be strongest near the bottom (Lentz and Chapman 2004). Figure 9 is rather consistent with this as are slope Burger numbers computed in section 3 [one should remain cautious though that the assumption of alongshore invariance essential in Lentz and Chapman (2004) may not apply well given the alongshore flow disruption by Cape Verde]. A scaling for upward velocities can thus be constructed as $w^{\mathrm{up}} \sim u_b \times s$, where s is the bottom slope and u_b is a typical, near-bottom, cross-shore velocity value. Based on mooring observations reported in this study and consistent with observations in other upwelling sectors a reasonable choice is $u_b = 5\,\mathrm{cm\,s^{-1}}$. Water parcels thus need around 10 days to travel from the shelf break to the midshelf upwelling zone, and, with a shelf slope around 2%, an estimate for w^{up} is $8\,\mathrm{m\,day^{-1}}$. This provides ample time for mixing episodes to take place along complex pathways that evolve under the influence of variable winds and mesoscale activity. As a result, upwelling dynamics may be more disrupted by IGWs in the SSUC than in other upwelling sectors (Schafstall et al. 2010; Avicola et al. 2007).

An unknown but presumably significant fraction of the energy driving mixing in the SSUC arises from the
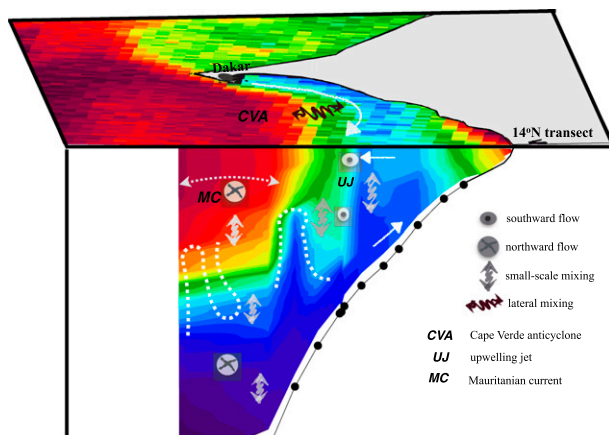
FIG. 15. 3D schematic description of the upwelling dynamical and hydrological structure over the southern Senegal shelf, as observed during UPSEN2–ECOAO. The manifestation of upwelling takes the form of a cold SST tongue situated tens of kilometers away the shore. Its position and that of its offshore frontal edge undergo cross-shore displacements influenced by mesoscale disturbances. These mesoscale disturbances presumably arise from instabilities of the current system composed of the poleward-flowing MC and the equatorward UJ. One recurrent mesoscale feature is the CVA, which strongly constrained the flow and hydrological conditions in the SSUC during the field experiment. Ubiquitous internal gravity waves over the shelf are implicated in water mass transformation (and associated vertical fluxes of properties) that occur offshore of the upwelling zone. In particular, interior mixing is frequently observed just offshore of the upwelling zone. Inshore of that zone, the classical 2D Ekman cell (onshore flow near the bottom, offshore flow in the surface layer) prevails. Therefore, the position of the upwelling zone may not simply result from the shutdown of the cross-shore Ekman-driven circulation on its inshore flank as in the 2D models of Estrade et al. (2008) and Austin and Lentz (2002). Partial evidence suggests that IGW breaking may contribute to the offshore migration of the front during UPSEN2–ECOAO. We hypothesize that the sharpness of the front separating upwelling and offshore waters is primarily controlled by IGW mixing in the front area, as opposed to lateral mixing resulting, for example, from submesoscale frontal dynamics (which has a limited signature in high-resolution SST images).

fission of internal tides into nonlinear internal waves that subsequently break and dissipate. The effect on vertical tracer fluxes is not known at present and depends on the distribution of IGW breaking aided by subinertial (Avicola et al. 2007) and possibly near-inertial shear. [The latter was also observed during the experiment (Fig. 9).] Based on studies for other shelves this effect deserves careful attention. In particular, it would be interesting to know the extent to which IGW breaking contributes to the enrichment of the shelf euphotic layer in nutrients through vertical diffusive fluxes. Relaxation periods when stratification recovers, or the establishment of the Cape Verde anticyclone, which enhances shelf stratification, are favorable to internal

wave activity and are thus presumably conditions in which these fluxes are particularly strong.

Thermohaline heterogeneities efficiently contribute to the disruption of IGW propagation. During UPSEN2 and the beginning of ECOAO, the upwelling front is well marked and impinges on the continental shelf. Preferential dissipation of IGWs in the offshore vicinity of the upwelling front is supported by many vertical tracer profiles. This has potentially important dynamical implications. Additional observations will be needed to further evaluate the significance of IGWs "pounding" on the upwelling front in its tendency to migrate offshore. The tentative energetic analysis presented in section 4 leads to upwelling front offshore displacements of a few hundred meters per day, which is modest (e.g., in regard to displacements associated with mesoscale disturbances), but uncertainties are large. A more qualitative element supporting the dynamical importance of IGW mixing is the sequence of satellite SST images during UPSEN2–ECOAO that show the progressive erosion of Cape Verde mesoscale anticyclones. Concomitant in situ observations reveal intense interior mixing undergone by the thermocline waters within the CVAs. Our interpretation is that CVAs bring substantial stratification over the shelf, which in turn allows IGWs to exist and progressively erode that stratification, that is, contribute to the CVA decay. On the other hand, SST images do not reveal significant submesoscale frontal activity in comparison to other situations; hence, lateral diffusive effects should be modest (Capet et al. 2008a).

Figure 15 helps summarize our main findings and results. The southern Senegal upwelling system is situated over a broad continental shelf. So far, study of this system has overwhelmingly relied on satellite images and has been focused on long time scales (seasonal to interannual; e.g., Lathuilière et al. 2008). The presence of Cape Verde and abrupt change of shelf width in its vicinity must conspire to produce quasi-permanent upwelling intensification just south of the cape, as also found in other upwelling regions, for example, near Capes Blanco and Mendocino in the California system. The in situ observations we present reveal the complexity and variability of the structure and functioning of the upwelling that is driven by synoptic wind variability, mesoscale effects, and possibly mixing due to superinertial wave activity.

The manifestations of mesoscale turbulence involve preferential and persistent patterns that connect the shelf and open-ocean environment and impact the shelf upwelling dynamics. Superinertial wave activity also seems important for the upwelling sector functioning. Our study provides some indications that internal tides and nonlinear internal gravity waves can play a systemic role in the SSUC through water mass transformation

and vertical flux of properties. In sustained upwelling conditions, where most of the subsurface water feeding the coastal divergence enters the shelf area in the northern SSUC and subsequently flows southward (S. Ndoye et al. 2016, manuscript submitted to *Geophys. Res. Lett.*), we expect the stratification to be increasingly impacted by IGWs toward the south (i.e., downstream with respect to the dominant shelf circulation), as we generally observe during UPSEN2–ECOAO. However, water residence time scales over the southern Senegal shelf are comparable to those of synoptic variability. Water property modifications and biogeochemical activity thus take place along complex pathways that integrate the influence of synoptic wind variability and mesoscale and internal tide activity. How much of that complexity needs to be accounted for to properly understand the ecological functioning of the SSUC (e.g., as a nursery for small pelagic fish) and its long-term evolution will be the subject of future research. Most urgently perhaps, the conditions in which very low dissolved oxygen levels develop over the shelf, as during the final part of UPSEN2–ECOAO experiments, need to be clarified.

REFERENCES

Adams, K. A., J. A. Barth, and F. Chan, 2013: Temporal variability of near-bottom dissolved oxygen during upwelling off central Oregon. *J. Geophys. Res. Oceans*, **118**, 4839–4854, doi:10.1002/jgrc.20361.

Alford, M. H., and R. Pinkel, 2000: Observations of overturning in the thermocline: The context of ocean mixing. *J. Phys. Oceanogr.*, **30**, 805–832, doi:10.1175/1520-0485(2000)030<0805:OOOITT>2.0.CO;2.

Allen, J., P. Newberger, and J. Federiuk, 1995: Upwelling circulation on the Oregon continental shelf. Part I: Response to idealized forcing. *J. Phys. Oceanogr.*, **25**, 1843–1866, doi:10.1175/1520-0485(1995)025<1843:UCOTOC>2.0.CO;2.

Aristegui, J., and Coauthors, 2009: Sub-regional ecosystem variability in the canary current upwelling. *Prog. Oceanogr.*, **83**, 33–48, doi:10.1016/j.pocean.2009.07.031.

Austin, J. A., and J. A. Barth, 2002: Variation in the position of the upwelling front on the Oregon shelf. *J. Geophys. Res.*, **107**, 3180, doi:10.1029/2001JC000858.

——, and S. J. Lentz, 2002: The inner shelf response to wind-driven upwelling and downwelling. *J. Phys. Oceanogr.*, **32**, 2171–2193, doi:10.1175/1520-0485(2002)032<2171:TISRTW>2.0.CO;2.

Avicola, G., J. N. Moum, A. Perlin, and M. D. Levine, 2007: Enhanced turbulence due to the superposition of internal gravity waves and a coastal upwelling jet. *J. Geophys. Res.*, **112**, C06024, doi:10.1029/2006JC003831.

Barton, E. D., 1989: The poleward undercurrent on the eastern boundary of the subtropical North Atlantic. *Poleward Flows Along Eastern Ocean Boundaries*, S. J. Neshyba et al., Eds., Springer, 82–95.

——, 1998: Eastern boundary of the North Atlantic: Northwest Africa and Iberia. *The Global Coastal Ocean: Regional Studies and Syntheses*, A. R. Robinson and K. H. Brink, Eds., The Sea—Ideas and Observations on Progress in the Study of the Seas, Vol. 11, John Wiley and Sons, 633–657.

——, A. Huyer, and R. L. Smith, 1977: Temporal variation observed in the hydrographic regime near Cabo Corveiro in the northwest African upwelling region, February to April 1974. *Deep-Sea Res.*, **24**, 7–23, doi:10.1016/0146-6291(77)90537-9.

Boccaletti, G., R. Ferrari, and B. Fox-Kemper, 2007: Mixed layer instabilities and restratification. *J. Phys. Oceanogr.*, **37**, 2228–2250, doi:10.1175/JPO3101.1.

Bretherton, F. P., R. E. Davis, and C. Fandry, 1976: A technique for objective analysis and design of oceanographic experiments applied to MODE-73. *Deep-Sea Res. Oceanogr. Abstr.*, **23**, 559–582, doi:10.1016/0011-7471(76)90001-2.

Capet, X., P. Marchesiello, and J. C. McWilliams, 2004: Upwelling response to coastal wind profiles. *Geophys. Res. Lett.*, **31**, L13311, doi:10.1029/2004GL020123.

——, E. J. Campos, and A. M. Paiva, 2008a: Submesoscale activity over the Argentinian shelf. *Geophys. Res. Lett.*, **35**, L15605, doi:10.1029/2008GL034736.

——, F. Colas, P. Penven, P. Marchesiello, and J. C. McWilliams, 2008b: Eddies in eastern boundary subtropical upwelling systems. *Ocean Modeling in an Eddying Regime, Geophys. Monogr.*, Vol. 177, Amer. Geophys. Union, 131–147.

——, J. C. McWilliams, M. J. Molemaker, and A. Shchepetkin, 2008c: Mesoscale to submesoscale transition in the California Current System. Part I: Flow structure and eddy flux. *J. Phys. Oceanogr.*, **38**, 29–43, doi:10.1175/2007JPO3671.1.

——, ——, ——, and ——, 2008d: Mesoscale to submesoscale transition in the California Current System. Part II: Frontal processes. *J. Phys. Oceanogr.*, **38**, 44–64, doi:10.1175/2007JPO3672.1.

Citeau, J., L. Finaud, J. Cammas, and H. Demarcq, 1989: Questions relative to ITCZ migrations over the tropical Atlantic Ocean, sea surface temperature and Senegal River runoff. *Meteor. Atmos. Phys.*, **41**, 181–190, doi:10.1007/BF01026109.

Crépon, M., C. Richez, and M. Chartier, 1984: Effects of coastline geometry on upwellings. *J. Phys. Oceanogr.*, **14**, 1365–1382, doi:10.1175/1520-0485(1984)014<1365:EOCGOU>2.0.CO;2.

Csanady, G. T., 1982: *Circulation in the Coastal Ocean.* Dordrecht, 279 pp.

Demarcq, H., and V. Faure, 2000: Coastal upwelling and associated retention indices derived from satellite SST. Application to *Octopus vulgaris* recruitment. *Oceanol. Acta*, **23**, 391–408, doi:10.1016/S0399-1784(00)01113-0.

Dillon, T., 1982: Vertical overturns: A comparison of Thorpe and Ozmidov length scales. *J. Geophys. Res.*, **87**, 9601–9613, doi:10.1029/JC087iC12p09601.

Ekman, V. W., 1905: On the influence of the earth's rotation on ocean currents. *Ark. Mat. Astron. Fys.*, **2**, 1–53.

Estrade, P., P. Marchesiello, A. Colin de Verdière, and C. Roy, 2008: Cross-shelf structure of coastal upwelling: A two-dimensional extension of Ekman's theory and a mechanism for inner shelf upwelling shut down. *J. Mar. Res.*, **66**, 589–616, doi:10.1357/002224008787536790.

Evans, W., B. Hales, P. G. Strutton, R. K. Shearman, and J. A. Barth, 2015: Failure to bloom: Intense upwelling results in negligible phytoplankton response and prolonged CO_2 out-gassing over the Oregon shelf. *J. Geophys. Res. Oceans*, **120**, 1446–1461, doi:10.1002/2014JC010580.

Flament, P., L. Armi, and L. Washburn, 1985: The evolving structure of an upwelling filament. *J. Geophys. Res.*, **90**, 11 765–11 778, doi:10.1029/JC090iC06p11765.

Fox-Kemper, B., R. Ferrari, and R. Hallberg, 2008: Parameterization of mixed layer eddies. I: Theory and diagnosis. *J. Phys. Oceanogr.*, **38**, 1145–1165, doi:10.1175/2007JPO3792.1.

Gan, J., and J. S. Allen, 2002: A modeling study of shelf circulation off northern California in the region of the coastal ocean dynamics experiment 2. Simulations and comparisons with observations. *J. Geophys. Res.*, **107**, 3184, doi:10.1029/2001JC0011902002.

——, A. Cheung, X. Guo, and L. Li, 2009: Intensified upwelling over a widened shelf in the northeastern South China Sea. *J. Geophys. Res.*, **114**, C09019, doi:10.1029/2007JC004660.

Gerkema, T., 1996: A unified model for the generation and fission of internal tides in a rotating ocean. *J. Mar. Res.*, **54**, 421–450, doi:10.1357/0022240963213574.

Holliday, D., and M. E. McIntyre, 1981: On potential energy density in an incompressible, stratified fluid. *J. Fluid Mech.*, **107**, 221–225, doi:10.1017/S0022112081001742.

Hughes, P., and E. Barton, 1974: Stratification and water mass structure in the upwelling area off northwest Africa in April/May 1969. *Deep-Sea Res. Oceanogr. Abstr.*, **21**, 611–628, doi:10.1016/0011-7471(74)90046-1.

Huyer, A., J. H. Fleischbein, J. Keister, P. M. Kosro, N. Perlin, R. L. Smith, and P. A. Wheeler, 2005: Two coastal upwelling domains in the northern California Current System. *J. Mar. Res.*, **63**, 901–929, doi:10.1357/002224005774464238.

Jackson, C., and J. R. Apel, 2009: *An Atlas of Internal Solitary-Like Waves and Their Properties.* Global Ocean Associates, 230 pp. [Available online at http://www.internalwaveatlas.com/Atlas_index.html.]

Jeans, D., and T. Sherwin, 2001: The evolution and energetics of large amplitude nonlinear internal waves on the Portuguese shelf. *J. Mar. Res.*, **59**, 327–353, doi:10.1357/002224001762842235.

Kang, D., and O. Fringer, 2010: On the calculation of available potential energy in internal wave fields. *J. Phys. Oceanogr.*, **40**, 2539–2545, doi:10.1175/2010JPO4497.1.

Kudela, R. M., and Coauthors, 2008: New insights into the controls and mechanisms of plankton productivity in coastal upwelling waters of the northern California Current System. *Oceanography*, **21**, 46–59, doi:10.5670/oceanog.2008.04.

Lamb, K. G., 2014: Internal wave breaking and dissipation mechanisms on the continental slope/shelf. *Annu. Rev. Fluid Mech.*, **46**, 231–254, doi:10.1146/annurev-fluid-011212-140701.

Lathuilière, C., V. Echevin, and M. Lévy, 2008: Seasonal and intraseasonal surface chlorophyll-a variability along the northwest African coast. *J. Geophys. Res.*, **113**, C05007, doi:10.1029/2007JC004433.

Lentz, S. J., 1992: The surface boundary layer in coastal upwelling regions. *J. Phys. Oceanogr.*, **22**, 1517–1539, doi:10.1175/1520-0485(1992)022<1517:TSBLIC>2.0.CO;2.

——, and D. C. Chapman, 2004: The importance of nonlinear cross-shelf momentum flux during wind-driven coastal upwelling. *J. Phys. Oceanogr.*, **34**, 2444–2457, doi:10.1175/JPO2644.1.

Li, Q., and D. M. Farmer, 2011: The generation and evolution of nonlinear internal waves in the deep basin of the South China Sea. *J. Phys. Oceanogr.*, **41**, 1345–1363, doi:10.1175/2011JPO4587.1.

Lucas, A. J., C. L. Dupont, V. Tai, J. L. Largier, B. Palenik, and P. J. Franks, 2011a: The green ribbon: Multiscale physical control of phytoplankton productivity and community structure over a narrow continental shelf. *Limnol. Oceanogr.*, **56**, 611–626, doi:10.4319/lo.2011.56.2.0611.

——, P. J. Franks, and C. L. Dupont, 2011b: Horizontal internal-tide fluxes support elevated phytoplankton productivity over the inner continental shelf. *Limnol. Oceanogr. Fluids Environ.*, **1**, 56–74, doi:10.1215/21573698-1258185.

——, G. C. Pitcher, T. A. Probyn, and R. M. Kudela, 2014: The influence of diurnal winds on phytoplankton dynamics in a coastal upwelling system off southwestern Africa. *Deep-Sea Res.*, **101**, 50–62, doi:10.1016/j.dsr2.2013.01.016.

Marchesiello, P., and P. Estrade, 2009: Eddy activity and mixing in upwelling systems: A comparative study of northwest Africa and California regions. *Int. J. Earth Sci.*, **98**, 299–308, doi:10.1007/s00531-007-0235-6.

——, J. C. McWilliams, and A. Shchepetkin, 2003: Equilibrium structure and dynamics of the California Current System. *J. Phys. Oceanogr.*, **33**, 753–783, doi:10.1175/1520-0485(2003)33<753:ESADOT>2.0.CO;2.

Messié, M., and F. P. Chavez, 2015: Seasonal regulation of primary production in eastern boundary upwelling systems. *Prog. Oceanogr.*, **134**, 1–18, doi:10.1016/j.pocean.2014.10.011.

Millot, C., and M. Crépon, 1981: Inertial oscillations on the continental shelf of the Gulf of Lions—Observations and theory. *J. Phys. Oceanogr.*, **11**, 639–657, doi:10.1175/1520-0485(1981)011<0639:IOOTCS>2.0.CO;2.

Morison, J., R. Andersen, N. Larson, E. D'Asaro, and T. Boyd, 1994: The correction for thermal-lag effects in Sea-Bird CTD data. *J. Atmos. Oceanic Technol.*, **11**, 1151–1164, doi:10.1175/1520-0426(1994)011<1151:TCFTLE>2.0.CO;2.

Moum, J., D. Farmer, W. Smyth, L. Armi, and S. Vagle, 2003: Structure and generation of turbulence at interfaces strained by internal solitary waves propagating shoreward over the continental shelf. *J. Phys. Oceanogr.*, **33**, 2093–2112, doi:10.1175/1520-0485(2003)033<2093:SAGOTA>2.0.CO;2.

——, ——, E. Shroyer, W. Smyth, and L. Armi, 2007: Dissipative losses in nonlinear internal waves propagating across the continental shelf. *J. Phys. Oceanogr.*, **37**, 1989–1995, doi:10.1175/JPO3091.1.

Ndoye, S., 2016: Fonctionnement dynamique du centre dupwelling sud-sénégalais: Approche par la modélisation réaliste et lanalyse dobservations satellite de température de la mer. Ph.D. thesis, Université Pierre et Marie Curie, 185 pp.

——, X. Capet, P. Estrade, B. Sow, D. Dagorne, A. Lazar, A. Gaye, and P. Brehmer, 2014: SST patterns and dynamics of the

southern Senegal-Gambia upwelling center. *J. Geophys. Res. Oceans*, **119**, 8315–8335, doi:10.1002/2014JC010242.

Osborn, T., 1980: Estimates of the local rate of vertical diffusion from dissipation measurements. *J. Phys. Oceanogr.*, **10**, 83–89, doi:10.1175/1520-0485(1980)010<0083:EOTLRO>2.0.CO;2.

Pallàs-Sanz, E., T. Johnston, and D. Rudnick, 2010: Frontal dynamics in a California Current System shallow front: 1. Frontal processes and tracer structure. *J. Geophys. Res.*, **115**, C12067, doi:10.1029/2009JC006032.

Palmer, M., G. Stephenson, M. Inall, C. Balfour, A. Düsterhus, and J. Green, 2015: Turbulence and mixing by internal waves in the Celtic Sea determined from ocean glider microstructure measurements. *J. Mar. Syst.*, **144**, 57–69, doi:10.1016/j.jmarsys.2014.11.005.

Pawlowicz, R., B. Beardsley, and S. Lentz, 2002: Classical tidal harmonic analysis including error estimates in MATLAB using T_TIDE. *Comput. Geosci.*, **28**, 929–937, doi:10.1016/S0098-3004(02)00013-4.

Peña-Izquierdo, J., J. L. Pelegrí, M. V. Pastor, P. Castellanos, M. Emelianov, M. Gasser, J. Salvador, and E. Vázquez-Domínguez, 2012: The continental slope current system between Cape Verde and the Canary Islands. *Sci. Mar.*, **76**, 65–78, doi:10.3989/scimar.03607.18C.

Pitcher, G., F. Figueiras, B. Hickey, and M. Moita, 2010: The physical oceanography of upwelling systems and the development of harmful algal blooms. *Prog. Oceanogr.*, **85**, 5–32, doi:10.1016/j.pocean.2010.02.002.

Pringle, J. M., 2002: Enhancement of wind-driven upwelling and downwelling by alongshore bathymetric variability. *J. Phys. Oceanogr.*, **32**, 3101–3112, doi:10.1175/1520-0485(2002)032<3101:EOWDUA>2.0.CO;2.

——, and E. P. Dever, 2009: Dynamics of wind-driven upwelling and relaxation between Monterey Bay and point arena: Local-, regional-, and gyre-scale controls. *J. Geophys. Res.*, **114**, C07003, doi:10.1029/2008JC005016.

Roullet, G., and P. Klein, 2009: Available potential energy diagnosis in a direct numerical simulation of rotating stratified turbulence. *J. Fluid Mech.*, **624**, 45–55, doi:10.1017/S0022112008004473.

Roy, C., 1998: An upwelling-induced retention area off Senegal: A mechanism to link upwelling and retention processes. *S. Afr. J. Mar. Sci.*, **19**, 89–98, doi:10.2989/025776198784126881.

Ryan, J., and Coauthors, 2010: Recurrent frontal slicks of a coastal ocean upwelling shadow. *J. Geophys. Res.*, **115**, C12070, doi:10.1029/2010JC006398.

Saha, S., and Coauthors, 2010: The NCEP Climate Forecast System Reanalysis. *Bull. Amer. Meteor. Soc.*, **91**, 1015–1057, doi:10.1175/2010BAMS3001.1.

Schafstall, J., M. Dengler, P. Brandt, and H. Bange, 2010: Tidal-induced mixing and diapycnal nutrient fluxes in the Mauritanian upwelling region. *J. Geophys. Res.*, **115**, C10014, doi:10.1029/2009JC005940.

Sharples, J., and Coauthors, 2007: Spring-neap modulation of internal tide mixing and vertical nitrate fluxes at a shelf edge in summer. *Limnol. Oceanogr.*, **52**, 1735–1747, doi:10.4319/lo.2007.52.5.1735.

Spall, M., 1997: Baroclinic jets in confluent flows. *J. Phys. Oceanogr.*, **27**, 1054–1071, doi:10.1175/1520-0485(1997)027<1054:BJICF>2.0.CO;2.

Strub, P. T., P. M. Kosro, and A. Huyer, 1991: The nature of the cold filaments in the California Current System. *J. Geophys. Res.*, **96**, 14 743–14 768, doi:10.1029/91JC01024.

Thompson, A. F., S. T. Gille, J. A. MacKinnon, and J. Sprintall, 2007: Spatial and temporal patterns of small-scale mixing in Drake Passage. *J. Phys. Oceanogr.*, **37**, 572–592, doi:10.1175/JPO3021.1.

Torgrimson, G. M., and B. M. Hickey, 1979: Barotropic and baroclinic tides over the continental slope and shelf off Oregon. *J. Phys. Oceanogr.*, **9**, 945–961, doi:10.1175/1520-0485(1979)009<0945:BABTOT>2.0.CO;2.

Tweddle, J. F., J. Sharples, M. R. Palmer, K. Davidson, and S. McNeill, 2013: Enhanced nutrient fluxes at the shelf sea seasonal thermocline caused by stratified flow over a bank. *Prog. Oceanogr.*, **117**, 37–47, doi:10.1016/j.pocean.2013.06.018.

Walter, R. K., M. E. Squibb, C. B. Woodson, J. R. Koseff, and S. G. Monismith, 2014: Stratified turbulence in the nearshore coastal ocean: Dynamics and evolution in the presence of internal bores. *J. Geophys. Res. Oceans*, **119**, 8709–8730, doi:10.1002/2014JC010396.

Wang, D.-P., and A. Jordi, 2011: Surface frontogenesis and thermohaline intrusion in a shelfbreak front. *Ocean Modell.*, **38**, 161–170, doi:10.1016/j.ocemod.2011.02.012.

Williams, C., J. Sharples, C. Mahaffey, and T. Rippeth, 2013: Wind-driven nutrient pulses to the subsurface chlorophyll maximum in seasonally stratified shelf seas. *Geophys. Res. Lett.*, **40**, 5467–5472, doi:10.1002/2013GL058171.

Woodruff, S., H. Diaz, J. Elms, and S. Worley, 1998: COADS Release 2 data and metadata enhancements for improvements of marine surface flux fields. *Phys. Chem. Earth*, **23**, 517–526, doi:10.1016/S0079-1946(98)00064-0.

Woodson, C., and Coauthors, 2007: Local diurnal upwelling driven by sea breezes in northern Monterey Bay. *Cont. Shelf Res.*, **27**, 2289–2302, doi:10.1016/j.csr.2007.05.014.

——, L. Washburn, J. A. Barth, D. Hoover, A. R. Kirincich, M. McManus, J. P. Ryan, and J. Tyburczy, 2009: Northern Monterey Bay upwelling shadow front: Observations of a coastally and surface-trapped buoyant plume. *J. Geophys. Res.*, **114**, C12013, doi:10.1029/2009JC005623.

Yu, L., and R. A. Weller, 2007: Objectively analyzed air–sea heat fluxes for the global ice-free oceans (1981–2005). *Bull. Amer. Meteor. Soc.*, **88**, 527–539, doi:10.1175/BAMS-88-4-527.